ADVANCED FUNCTIONAL MATERIALS
www.afm-journal.de

# Catalytic Oxidation of BTX (Benzene, Toluene, and Xylene) Using Metal Oxide Perovskites

*Jianhua Yuan, Guixiang Li, Xiao Liu, Yun Yang, Fei Yu, Jianglin Cao, Zhaofu Fei,* Jie Ma,* Mohammad K. Nazeeruddin,* and Paul J. Dyson**

**The high toxicity, volatility, and dispersion of the light aromatics, benzene, toluene, and xylene (BTX) pose a serious threat to the environment and human health. Compared to incineration, catalytic oxidation technologies for BTX removal offer benefits such as low energy consumption, high efficiency, and low pollution. $ABO_3$–type perovskite catalysts ($ABO_3$–PCs) are particularly promising materials for the catalytic oxidation of BTX due to their high activity and thermal stability, as well as their adjustable elemental composition and flexible structure allowing their properties to be improved. Nonetheless, the full potential of $ABO_3$–PCs for the oxidation of BTX has yet to be reached. This review systematically and critically analyses progress in the catalytic oxidation of BTX by $ABO_3$–PCs. Catalytic performance is assessed for each category of perovskite, including non–doped, doped (A–, B–, or A/B–site doped), and loading type (noble metal, metal oxide, and matrix composite), with structure–activity relationships are established. A kinetic model and proposed mechanism for the catalytic oxidation of BTX are also presented. Finally, the challenges and opportunities of $ABO_3$–PCs applied to BTX oxidation and other reactions are highlighted.**

## 1. Introduction

Volatile organic compounds (VOCs) are typically toxic and pathogenic, posing significant threats to both the natural environment and human health.[1] VOCs comprise hydrocarbons, ketones, aldehydes, etc. Among them, a group of light aromatic hydrocarbons known as BTX (benzene, toluene, and xylene) is considered highly polluting due to their significant contribution to photochemical reactions and ozone pollution.[2] As industrial VOC emission regulations become more stringent, the reduction and control of VOCs in many countries has become a key priority in air pollution management.[3] Notably, BTX, primarily originating from industrial processes such as synthetic rubber manufacture, paint and dye production, fiber synthesis, petroleum processing, semiconductor fabrication, and fuel production, have garnered attention due to their high toxicity and facile entry into the human body through inhalation or contact with skin.[4]

Recycling and removal are the two main methods of disposing BTX.[5] Recovery technologies are ideal for removing low–concentrations of BTX and offer advantages such as high efficiency and operational simplicity.[6] Nevertheless, additional treatments may be required to address potential secondary contamination.[7] Destruction technologies effectively treat BTX across a wide concentration range, completely breaking them down into harmless small molecules.[8] Biological and photocatalytic approaches remain in the development stages, and direct oxidation is only suitable for treating exhaust gases with a high combustible content.[9] Considering the economic and technical advantages of various treatment methods, catalytic oxidation has consistently offered low costs and high removal rates, positioning

J. Yuan, J. Cao, J. Ma
Research Center for Environmental Functional Materials
College of Environmental Science and Engineering
Tongji University
1239 Siping Road, Shanghai 200092, P. R. China
E-mail: jma@tongji.edu.cn

G. Li, Z. Fei, M. K. Nazeeruddin, P. J. Dyson
Institute of Chemical Sciences and Engineering
École Polytechnique Fédérale de Lausanne (EPFL)
Lausanne CH-1015, Switzerland
E-mail: zhaofu.fei@epfl.ch; mdkhaja.nazeeruddin@epfl.ch; paul.dyson@epfl.ch

X. Liu, Y. Yang
Shanghai Baoye Engineering Technology Ltd.
77 Anqing Road, Shanghai 200941, P. R. China

F. Yu
College of Marine Ecology and Environment
Shanghai Ocean University
Shanghai 201306, P. R. China

J. Ma
School of Civil Engineering
Kashi University
Kashi 844000, P. R. China

The ORCID identification number(s) for the author(s) of this article can be found under https://doi.org/10.1002/adfm.202401281



**DOI: 10.1002/adfm.202401281**

it as an efficient, environmentally friendly, and cost–effective approach for BTX removal.[10]

Catalytic oxidation methods offer a means of achieving complete oxidation, utilizing a catalyst to accelerate the oxidation process of BTX at temperatures of 300–500 °C.[11,12] This approach reduces energy consumption and allows the treatment of a wide range of BTX concentrations.[13] Typically, catalytic oxidation technologies achieve organic waste gas degradation rates exceeding 95%, with $CO_2$ and $H_2O$ serving as the final decomposition products. Additionally, the lower reaction temperatures employed in catalytic oxidation significantly suppresses $NO_x$ production, thereby surpassing other treatment methods.[14]

In recent years, there has been growing interest on the full oxidation of BTX, with a particular emphasis on developing novel catalysts.[15] Various catalysts, including noble metal–based and non–precious metal oxide catalysts, have been reported. However, there is a need for further improvement in terms of low–temperature catalytic activity and enhanced stability.[16,17] $ABO_3$–PCs have attracted attention as they possess high activity at low–temperatures, high stability and have easily adjustable redox properties.[18,19] Metal oxide perovskites follow the general formula $ABO_3$, where A represents rare earth ($La^{3+}$, $Sr^{2+}$, $Ce^{4+}$, $Sm^{2+}$, $Gd^{2+}$ etc.), alkali metal ions ($K^+$, $Rb^+$, $Cs^+$ etc.), or alkaline-earth ions ($Be^{2+}$, $Mg^{2+}$, $Ca^{2+}$, $Ba^{2+}$ etc.) and B represents transition metal ions ($Co^{2+}$, $Mn^{3+}$, $Ni^{3+}$, and $Fe^{2+}$ etc.).[20] The unique $ABO_3$ crystal structure, electronic structure, and other properties, make them highly promising as alternative catalysts due to their comparatively low cost.[21] There has been a steady increase in studies focusing on $ABO_3$–catalyzed oxidation of BTX,[22] with research focusing on understanding the factors that influence activity, providing mechanistic insights and ultimately catalyst design strategies. Notably, substitution of cations, either on the A– or B–site, with cations with similar radii, is a common strategy used to generate defects and oxygen vacancies that enhance catalytic performance.[23] Compared to many noble metal–based catalysts, $ABO_3$–PCs have large specific surface areas, rendering them highly active and cost–effective.[24]

Previous reviews on catalytic oxidation of VOCs have primarily focused on noble metal catalysts and non–precious metal catalysts.[25] A systematic review of the catalytic oxidation of BTX pollutants by $ABO_3$–PCs is lacking.[14] In this review, we address this gap by covering the advances made in the oxidation of BTX using $ABO_3$–PCs since the year 2000, providing a comprehensive understanding of the fundamental principles governing the catalytic oxidation of BTX.[26] The review begins by summarizing the sources and hazards of BTX and highlights the key features and advantages of $ABO_3$–catalyzed oxidation as a method to eliminate them. We evaluate the catalytic performance of $ABO_3$–PCs based on various categories, including non–doped, doped (A–site, B–site, and A/B–site doped), and different loading types (noble metal, metal oxide, and matrix composite). Additionally, the effects of overall morphology, structure, water vapor, and sulfur species on $ABO_3$–PCs are examined. The review also presents a systematic summary of the kinetic model and possible oxidation mechanism of BTX catalytic oxidation. Current issues and challenges are highlighted. Special emphasis is placed on outlining future research directions and prioritizing work in the field of BTX removal using $ABO_3$–PCs. By providing a comprehensive and insightful overview, we believe the review will unlock additional opportunities to deepen the understanding of $ABO_3$ oxidation principles and lay the theoretical groundwork for developing new high–performance $ABO_3$–PCs.

## 2. BTX Sources and Hazards

BTX (benzene, toluene, and xylene) are a class of highly irritating and toxic organic compounds that fall under the category of volatile organic compounds (VOCs). These compounds are structurally stable aromatic compounds and are either non–polar (benzene) or weakly polar (toluene and xylene). The emission of BTX contribute significantly to global atmospheric pollution.[27] Consequently, BTX pose a threat to the environment and human health.[28]

### 2.1. Benzene

Benzene emissions primarily originate from industrial activities, transportation, and fuel consumption.[29] There are three main sources of benzene:

i) Production processes – benzene is extensively used in the manufacture of synthetic rubber, plastics, paints, dyes, and other chemicals. Significant amounts of benzene are also generated during oil refining and fuel processing.[30]
ii) Transportation – benzene is present in vehicle exhaust, and is particularly prevalent in urban areas with a high traffic density.
iii) Tobacco – smoking releases benzene and other harmful substances, making it a significant sources of benzene emissions.

Benzene has various detrimental effects on the human body.[31] Benzene is myelotoxic and increases the risk of leukemia, lymphoma, and other forms of cancer. Long–term exposure to benzene can result in neurological damage, decreased mental capacity, and impaired immune system function, leading to the development of allergies, asthma, and other respiratory diseases.[32] Prolonged exposure to benzene during pregnancy can cause fetal malformations and miscarriages. Benzene can adversely affect the central nervous system, cardiovascular health, liver, lungs, kidneys, and other vital organs, giving rise to various secondary effects.[33,34]

### 2.2. Toluene

Toluene is primarily released through industrial pollution and urban traffic. Petrochemical processes, automobile exhaust, printing and lacquer industry, and synthetic wood and furniture panels, are among the sources of toluene emissions.[35] Toluene is carcinogenic and can cause irritation to the eyes and throat, respiratory irritation, as well as cause sensory abnormalities.[26] Exposure to high concentrations of toluene can result in symptoms such as headaches, dizziness, nausea, vomiting, and weakness, affecting the nervous system, liver, kidneys, immune system, and other organs. Prolonged exposure to toluene can lead to neurological and immune system disorders, including epilepsy, neuralgia, and anemia.[36]

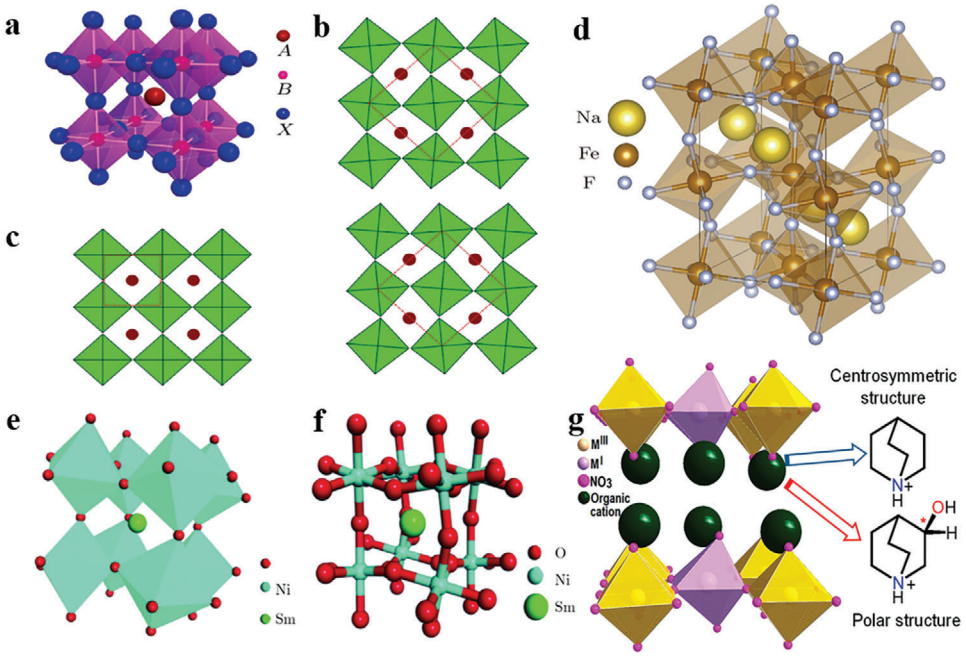


**Figure 1.** a–c) Three typical structures of $ABO_3$–type perovskites, d,e) inorganic, f) organic, and g) organic–inorganic perovskites.[40,41]

### 2.3. Xylenes

Xylene (*o*–, *m*– and *p*–xylene) is sourced from petroleum refining, printing and dyeing, plastic processing, and paint production.[6] It is also present in household items including perfumes, paints, and cleaners as well as in gasoline and diesel fuels. Exposure to xylene in the atmosphere poses risks to the central nervous system, respiratory system, and eyes.[25] Longer–term exposure to xylene can result in nausea, insomnia, headaches, and gastrointestinal discomfort,[37] and ultimately causes organ damage, cancer, and immunosuppression.[38] Xylene is also released into aquatic environments through industrial wastewater and municipal sewage, posing a threat to aquatic organisms and other ecological environments. It can also interact with other hazardous substances, leading to synergistic effects that pose an even greater threat to human health.[39]

## 3. Characteristics and Advantages of $ABO_3$–Type Perovskites

The general formula for a typical chalcogenide oxide is $ABO_3$, where lanthanide and/or alkaline earth metal ions, primarily located in the A–site, are combined with transition metal ions in the B–site, see **Figure 1**a–c. $ABO_3$–type perovskites have been evaluated in many fields, such as electrode materials in electrochemistry, advanced oxidation catalysis and as automotive exhaust gas catalysts.[40,41] Figure 1d–g illustrates typical inorganic, organic and organic–inorganic $ABO_3$ structures. With their unique structures and properties, $ABO_3$–type perovskites are promising catalysts for BTX oxidation.

$ABO_3$–PCs have the following characteristics that make them ideally suited to BTX oxidation.

i. High flexibility in composition. Studies have shown that approximately 90% of the metal ions in $ABO_3$–PCs can be substituted without altering the lattice structure, allowing for a certain degree of anionic or cationic defects.[42] The A– and B–sites of $ABO_3$ allows various types of dopants to be incorporated, so different types of functional catalysts may be prepared by doping different metal ions at the A– and B–sites.[43] Even the oxygen vacancies can be doped to some extent with $F^-$, $Cl^-$, and $S^{2-}$, further enhancing the flexibility of their components and thus potentially improving the performance in catalytic oxidation reactions.[44]
ii. Tunable redox properties. The excellent redox properties of $ABO_3$–PCs are predominantly associated with the rich valency of B–site transition metal ions,[45] which gives rise to lattice vacancies and/or alterations in the valence state of B–site ions upon substitution, providing $ABO_3$–PCs with a flexible and adjustable electronic structure.[46] Furthermore, although the A–site cation in $ABO_3$ is typically considered inert in catalytic reactions, it can influence the redox properties of $ABO_3$ by affecting the electroni'c structure, defect structure and surface properties of the B–site cation.[47]
iii. Oxygen migration properties.[48] $ABO_3$–PCs possess a high oxygen adsorption capacity affording two oxygen species, i.e., $\alpha$– and $\beta$–oxygen. $\alpha$–Oxygen refers to oxygen weakly adsorbed on the $ABO_3$ surface and $\beta$–oxygen corresponds to lattice oxygen within $ABO_3$. Due to the flexible composition and abundant defects in $ABO_3$, both $\alpha$– and $\beta$–oxygen can undergo rapid migration on the surface and in the bulk phase, thus improving the catalytic reaction rate of oxidation reactions. Moreover, oxygen mobility in $ABO_3$–PCs can be significantly enhanced by substitution of A and B sites. By increasing the oxygen mobility, the concentration of $\alpha$–oxygen

at the interface can be elevated, further improving catalytic activity.[49]

iv. Versatile surface properties. The $ABO_3$–PC motif can serve as a substrate for the generation of nanoparticles (NPs).[50] Specifically, selected metal elements can be initially doped into the chalcogenide lattice, and then, through reduction or high temperature processes, NPs can be formed on the $ABO_3$ surface.[51] Alternatively, $ABO_3$ can be loaded onto the surface of other substrates, such as zeolites, polymers and other metal oxides, taking advantage of the strong interactions between $ABO_3$ and other substances, thereby enhancing their performance as heterogeneous catalysts for the oxidation of pollutants.[52]

v. Anti–coking and anti–poisoning properties. $ABO_3$–PCs exhibit exceptional anti–coking properties during catalytic oxidation, ensuring thorough pollutant oxidation.[53] Notably, even when pure methane is used as a substrate, coke formation is not observed at high temperatures when employing $ABO_3$–PCs. Moreover, doping anions into the oxygen sites enables the chalcogenide lattice to act as a storage material for impurities such as sulfide and chloride, removing these species from the $ABO_3$ surface and improving tolerance to these catalyst poisons.[54] The outstanding oxygen and water storage capacity of $ABO_3$–PCs also contributes to their anti–coking and anti–poisoning properties.[55]

$ABO_3$–PCs offer several advantages for the catalytic oxidation of pollutants.

i. Facile and inexpensive preparation. The methods used to prepare $ABO_3$–PCs are straightforward and the preparation costs are relatively low.[56] Typically, hydrothermal, sol–gel and precipitation methods are used and require inexpensive precursors. Moreover, the methods are scalable, allowing $ABO_3$–PCs to be produced in large quantities.

ii. High activity. Due to the unique crystal structure and abundant oxygen vacancies, $ABO_3$–PCs exhibit remarkable oxidation activity and enable catalytic reactions to proceed at comparatively low temperatures and pressures.[57]

iii. Outstanding stability. $ABO_3$–PCs demonstrate exceptional stability even at high temperatures and pressures, ensuring sustained catalytic efficiency over extended periods and enabling recycling and reuse,[58] including under oxidative environments.[59]

iv. Sustainability. $ABO_3$–PCs are often free from toxic and harmful components, and their application also eliminates the need for using corrosive reagents, thereby ensuring an environmentally benign approach.[60]

## 4. $ABO_3$–PCs for BTX Oxidation

### 4.1. Non–Doped $ABO_3$–PCs

Non–doped perovskites, particularly La–based $ABO_3$–PCs, have been extensively investigated for their structural stability and compositional versatility. La–based $ABO_3$–PCs are excellent catalysts for various reactions, principally in the reduction of aldehydes and ketones, but also in the oxidation of BTX. Spinicci et al. investigated the oxidation of benzene using $LaMnO_3$ and $LaCoO_3$, with the former having a higher activity (a 20 °C difference in $T_{50\%}$). Redox analysis confirmed that cobalt in $LaCoO_3$ is exclusively in the $Co^{3+}$ oxidation state, whereas $LaMnO_3$ contains 35% $Mn^{4+}$ in addition to $Mn^{3+}$. Hence, the metal ion and valence state in the B–site have a significant influence on catalytic performance.[61] In a related study, Zhang et al. synthesized $LaMnO_3$ (LMO) using citric acid sol–gel (SG), glycine oxidation (GC) and co–precipitation (CP) techniques, and applied the perovskites in the oxidation of toluene. The catalytic activity followed the trend LMO–SG > LMO–CP > LMO–GC, aligning with the specific surface area of the catalyst and concentration of surface adsorbed oxygen species.[62] Rezlescu et al. compared $GdAlO_3$, $SrMnO_3$, $SrCoO_3$, and $MnFeO_3$ prepared using a sol–gel auto–combustion method in the complete oxidation of benzene. $SrMnO_3$ showed the highest catalytic activity at low temperatures. The differences in catalytic activity were attributed to the distinct reactivity of oxygen species involved and/or variations in the number of active sites on the perovskite surface.[63] **Table 1** provides an overview of non–doped $ABO_3$ compounds evaluated as catalysts for benzene and toluene oxidation over the past two decades. $LaCoO_3$, $LaMnO_3$, and $LaFeO_3$ have been extensively investigated, and further development of other non–doped $ABO_3$ species appear warranted. As observed from Table 1, the conversion temperature and performance of non–doped $ABO_3$–PCs differ, primarily influenced by the air velocity, benzene and toluene concentrations and other reaction conditions.

### 4.2. Stoichiometrically Doped and Defective $ABO_3$–PCs

The catalytic activity of $ABO_3$–PCs may be improved by replacing ions with radii similar to those in the A–, B–, and O-sites.[90] Catalytic activity is primarily attributed to the B–site cations, whereas the A–site cations mainly play a role in stabilizing the structure.[91] However, substituting an A–site cation with other metal ions potentially leads to an alteration in oxidation state, oxygen vacancies, and cation defect density of the B–site cation, ultimately affecting the catalytic performance. Therefore, the catalytic activity of $ABO_3$–PCs can be modified by introducing other ions through partial or simultaneous substitution of A– and B–site cations.[92] **Table 2** summarizes all doped $ABO_3$–PCs evaluated in the catalytic oxidation of BTX.

#### *4.2.1. A–Site Cation Doping*

The A–site ions of $ABO_3$–PCs play a pivotal role in stabilizing the structure by controlling the dispersion state and atomic valence of the active B–site component.[60] Despite the A–site ions having little direct involvement in chemical reactions, the substitution of the A–site ions indirectly influences the valence state of the B–site ions.[120] They can also introduce lattice defects and modify the chemical sites of the lattice oxygen, influencing the reactivity at B–sites.[121] A–site ions and $O^{2-}$ form a dense stacking layer dominated by ionic bonding.[122] Transition metals have multiple valences, which facilitates the variable substitution of the A–site ions, but can induce a change in the coordination number or lead to other structural changes.[123]

Parvizi et al. investigated the catalytic activity of $La_{0.8}A_{0.2}MnO_3$ (A: $Co^{2+}$, $Zn^{2+}$, $Mg^{2+}$, and $Ba^{2+}$) nanocatalysts in toluene

 

**Table 1.** Non–doped $ABO_3$–PCs evaluated in the catalytic oxidation of benzene and toluene.

| Catalyst | Reactant composition | Space velocity/flow rate | $T_{50\%}$ [°C] | $T_{90\%}$ [°C] | References |
|---|---|---|---|---|---|
| $LaMnO_3$ | $C_6H_6$ /$O_2$:1/100 | 14100 mL $g^{-1}$ $h^{-1}$ | 301 | – | [61] |
| $LaCoO_3$ | $C_6H_6$ /$O_2$:1/100 | 14100 mL $g^{-1}$ $h^{-1}$ | 323 | – | [61] |
| $GdAlO_3$ | 1–2% $C_7H_8$ | 5100 mL $g^{-1}$ $h^{-1}$ | 350 | – | [61] |
| $SrMnO_3$ | 1–2% $C_7H_8$ | 20000 mL $g^{-1}$ $h^{-1}$ | 325 | – | [64] |
| $LaCoO_3$ | 500 ppm $C_6H_6$ | 96000 mL $g^{-1}$ $h^{-1}$ | 266 | 331 | [65] |
| $LaCoO_3$ | 500 ppm $C_6H_6$ | 96000 mL $g^{-1}$ $h^{-1}$ | 288 | 388 | [66] |
| $LaNiO_3$ | 400 ppm $C_6H_6$ | 100 mL $min^{-1}$ | ≈350 | – | [67] |
| $LaMnO_3$ | 400 ppm $C_6H_6$ | 100 mL $min^{-1}$ | ≈250 | – | [67] |
| $LaFeO_3$ | 400 ppm $C_6H_6$ | 100 mL $min^{-1}$ | ≈420 | – | [67] |
| $LaCoO_3$ | 400 ppm $C_6H_6$ | 100 mL $min^{-1}$ | ≈390 | – | [68] |
| $LaCoO_3$ | 500 ppm $C_7H_8$ | 192000 mL $g^{-1}$ $h^{-1}$ | – | 275 | [69] |
| $LaMnO_3$–SG | 1000 ppm $C_7H_8$ | 15000 mL $g^{-1}$ $h^{-1}$ | 204 | 224 | [62] |
| $LaMnO_3$–GC | 1000 ppm $C_7H_8$ | 15000 mL $g^{-1}$ $h^{-1}$ | 245 | 274 | [62] |
| $LaMnO_3$–CP | 1000 ppm $C_7H_8$ | 15000 mL $g^{-1}$ $h^{-1}$ | 214 | 257 | [62] |
| $LaFeO_3$ | 210 ppm $C_7H_8$ | 138 mL·$min^{-1}$ | 506 | 545 | [70] |
| $LaCoO_3$–acetic acid | 1000 ppm $C_7H_8$ | 60000 mL $g^{-1}$ $h^{-1}$ | – | 223 | [71] |
| $LaFeO_3$–5 | 1000 ppm $C_7H_8$ | 20000 mL $g^{-1}$ $h^{-1}$ | 255.9 | 277.3 | [72] |
| $LaFeO_3$ | 1000 ppm $C_7H_8$ | 20000 mL $g^{-1}$ $h^{-1}$ | – | 243 | [63] |
| $LaFeO_3$ | 1000 ppm $C_7H_8$ | 20000 mL $g^{-1}$ $h^{-1}$ | 308.1 | 333.3 | [73] |
| $SrTiO_3$ | 1000 ppm $C_7H_8$ | 100 mL $min^{-1}$ | 370 | 385 | [74] |
| $LaMnO_3$ | 1000 ppm $C_7H_8$ | 60000 mL $g^{-1}$ $h^{-1}$ | 229 | 298 | [75] |
| $LaMnO_3$ | 1000 ppm $C_7H_8$ | 100 mL $min^{-1}$ | 295 | 332 | [76] |
| $LaFeO_3$ | 4000 ppm $C_7H_8$ | 47000 mL $g^{-1}$ $h^{-1}$ | 323 | – | [77] |
| $LaNiO_3$ | 4000 ppm $C_7H_8$ | 47000 mL $g^{-1}$ $h^{-1}$ | 297 | – | [77] |
| $LaMnO_3$ | 5 g $m^{-3}$ $C_7H_8$ | 18000 mL $g^{-1}$ $h^{-1}$ | 170 | 250 | [78] |
| $LaCoO_3$ | 1000 ppm $C_7H_8$ | 100 mL $min^{-1}$ | 268 | 411 | [79] |
| Bulk–$LaMnO_3$ | 1000 ppm $C_7H_8$ | 20000 mL $g^{-1}$ $h^{-1}$ | 263 | 300 | [80] |
| $SmMnO_3$ | 1000 ppm $C_7H_8$ | 48000 mL $g^{-1}$ $h^{-1}$ | 223 | 258 | [81] |
| $SmMnO_3$ | 1000 ppm $C_7H_8$ | 24000 mL $g^{-1}$ $h^{-1}$ | – | <240 | [82] |
| $LaMnO_3$ | 1000 ppm $C_7H_8$ | 40000 mL $g^{-1}$ $h^{-1}$ | 281 | 290 | [83] |
| $LaFeO_3$ | 0.2 mol% $C_7H_8$ | 15000 mL $g^{-1}$ $h^{-1}$ | 268 | 400 | [84] |
| $GdMnO_3$ (SY)–0.05 | 1000 ppm $C_7H_8$ | 60000 mL $g^{-1}$ $h^{-1}$ | 240 | 260 | [85] |
| $GdMnO_3$ (SY) | 1000 ppm $C_7H_8$ | 60000 mL $g^{-1}$ $h^{-1}$ | 244 | 276 | [85] |
| $LaMnO_3$ | 1000 ppm $C_7H_8$ | 100 mL $min^{-1}$ | 349 | 416 | [86] |
| $LaFeO_3$ | 0.1 vol% $C_7H_8$ | 20000 mL $g^{-1}$ $h^{-1}$ | 200 | 253 | [87] |
| $LaCoO_3$ | 1000 ppm $C_7H_8$ | 20000 mL $g^{-1}$ $h^{-1}$ | – | >280 | [88] |
| $LaCrO_3$ | 1000 ppm $C_7H_8$ | 9600 mL $g^{-1}$ $h^{-1}$ | 352 | 445 | [89] |

if oxygen is not mentioned in the list, then the reaction system uses air.

oxidation and found that $La_{0.8}Zn_{0.2}MnO_3$ exhibited the highest activity (**Figure 2a**).[124] Similarly, Liu et al. synthesized $La_{1-x}Ce_xMnO_3$ (x = 0–10%) doped perovskites and observed that $Ce^{4+}$ substitution increased the $Mn^{4+}/Mn^{3+}$ ratio and oxygen species, resulting in enhanced catalytic activity (Figure 2b).[93] In another study, Liu et al. prepared $La_{1-x}Ce_xMnO_3$ (x = 0–10%) using flame spray pyrolysis and investigated their activity in the catalytic oxidation of benzene at temperatures ranging from 100 to 450 °C. The introduction of $Ce^{4+}$ resulted in a change in the chemical state of B–site ions and oxygen species, with the ratios of $Mn^{4+}/Mn^{3+}$ and the adsorbed oxygen/lattice oxygen ($O_{ads}/O_{latt}$) ratio on the catalyst surface increasing, and enhancing catalytic activity.[125]

$SmMnO_3$, $Sm_{0.8}A_{0.2}MnO_3$ (A = Ce, Sr, and Ca), and $Sm_{1-x}Ca_xMnO_3$ (x = 0.0, 0.1, 0.2, and 0.3) were synthesized via a sol–gel method and evaluated in the catalytic oxidation of toluene in a fixed–bed reactor. Substitution of $Ce^{4+}$ and $Ca^{2+}$ positively influences the catalytic performance in toluene oxidation,[94] whereas the substitution of $Sr^{2+}$ has a negative effect (Figure 2c). Zhao et al. used porous $La_{1-x}Co_xFeO_3$ (x = 0–0.4) for toluene oxidation.[126] Partial substitution of $La^{3+}$ by $Co^{3+}$ in $LaFeO_3$ induced structural deformations, increasing its specific surface

**Table 2.** Doped $ABO_3$–PCs employed in the catalytic oxidation of BTX.

| Catalyst | Reactant composition | Space velocity/flow rate | $T_{50\%}$ [°C] | $T_{90\%}$ [°C] | References |
|---|---|---|---|---|---|
| $La_{0.8}Sr_{0.2}MnO_{3-\delta}$ | 500 ppm $C_6H_6$ | 20000 mL $g^{-1}$ $h^{-1}$ | 520 | – | [33] |
| $LaCoO_3$ | 500 ppm $C_6H_6$ | 96000 mL $g^{-1}$ $h^{-1}$ | 266 | 331 | [65] |
| $La_{1-x}Sr_xMnO_3$ | 400 ppm $C_6H_6$ | 100 mL $min^{-1}$ | ≈270 | – | [68] |
| $SrTi_{1-X}CuXO_3$ | 1000 ppm $C_7H_8$ | 100 mL $min^{-1}$ | 348 | 412 | [74] |
| $SrTi_{1-X}MnXO_3$ | 1000 ppm $C_7H_8$ | 100 mL $min^{-1}$ | 305 | 335 | [74] |
| $La_{0.8}Ca_{0.2}FeO_3$ | 4000 ppm $C_7H_8$ | 47000 mL $g^{-1}$ $h^{-1}$ | 289 | – | [77] |
| $La_{0.8}Ca_{0.2}NiO_3$ | 4000 ppm $C_7H_8$ | 47000 mL $g^{-1}$ $h^{-1}$ | 333 | – | [77] |
| $La_{0.6}Ca_{0.4}NiO_3$ | 4000 ppm $C_7H_8$ | 47000 mL $g^{-1}$ $h^{-1}$ | 346 | – | [77] |
| $LaCo_{0.6}Fe_{0.4}O_3$ | 1000 ppm $C_7H_8$ | 100 mL $min^{-1}$ | 218 | 363 | [79] |
| $LaCo_{0.6}Cr_{0.4}O_3$ | 1000 ppm $C_7H_8$ | 100 mL $min^{-1}$ | 242 | 384 | [79] |
| $LaCo_{0.6}Cu_{0.4}O_3$ | 1000 ppm $C_7H_8$ | 100 mL $min^{-1}$ | 261 | 410 | [79] |
| $LaZn_{0.01}Fe_{0.99}O_3$ | 0.2 mol% $C_7H_8$ | 15000 mL $g^{-1}$ $h^{-1}$ | 235 | 363 | [84] |
| $LaZn_{0.05}$ $Fe_{0.95}O_3$ | 0.2 mol% $C_7H_8$ | 15000 mL $g^{-1}$ $h^{-1}$ | 233 | 356 | [84] |
| $LaZn_{0.1}Fe_{0.9}O_3$ | 0.2 mol% $C_7H_8$ | 15000 mL $g^{-1}$ $h^{-1}$ | 230 | 335 | [84] |
| $LaZn_{0.2}Fe_{0.8}O_3$ | 0.2 mol% $C_7H_8$ | 15000 mL $g^{-1}$ $h^{-1}$ | 226 | 327 | [84] |
| $LaZn_{0.3}Fe_{0.7}O_3$ | 0.2 mol% $C_7H_8$ | 15000 mL $g^{-1}$ $h^{-1}$ | 222 | 323 | [84] |
| $La_{0.67}Ca_{0.33}CrO_3$ | 1000 ppm $C_7H_8$ | 9600 mL $g^{-1}$ $h^{-1}$ | 302 | 381 | [89] |
| $La_{0.8}Ca_{0.2}CrO_3$ | 1000 ppm $C_7H_8$ | 9600 mL $g^{-1}$ $h^{-1}$ | 354 | 424 | [89] |
| $La_{0.5}Ca_{0.5}CrO_3$ | 1000 ppm $C_7H_8$ | 9600 mL $g^{-1}$ $h^{-1}$ | 295 | 374 | [89] |
| $La_{1-x}Ce_xMnO_3$ | 1000 ppm $C_6H_6$ | 60000 mL $g^{-1}$ $h^{-1}$ | – | 450 | [93] |
| $Sm_{0.8}Ca_{0.2}MnO_3$ | 1000 ppm $C_7H_8$ | 100 mL $min^{-1}$ | – | 238 | [94] |
| $La_{0.9}S_{r0.1}CoO_3$ | 1000 ppm $C_7H_8$ | 100 mL $min^{-1}$ | 219 | – | [95] |
| $LaNi_{0.75}Co_{0.25}O_3$ | 1000 ppm $C_7H_8$ | 18000 mL $g^{-1}$ $h^{-1}$ | – | 225 | [96] |
| $La_{0.5}Sr_{0.5}Co_{0.8}Fe_{0.2}O_{3-\delta}$ | 1000 ppm $C_7H_8$ | 30000 mL $g^{-1}$ $h^{-1}$ | 251 | 270 | [97] |
| $La_{0.8}Ce_{0.2}Mn_{0.8}Ni_{0.2}O_3$ | 1000 ppm $C_7H_8$ | 18000 mL $g^{-1}$ $h^{-1}$ | – | 295 | [98] |
| $La_{0.7}Sr_{0.3}Co_{0.8}Fe_{0.2}O_3$ | 500 ppm $C_7H_8$ | 5700 mL $g^{-1}$ $h^{-1}$ | >243 | – | [99] |
| $La_{0.8}Zn_{0.2}MnO_3$ | 1393 ppm $C_6H_6$ | 200 mL $min^{-1}$ | ≈400 | – | [100] |
| $La_{0.8}Zn_{0.2}MnO_3$ | 498 ppm $C_6H_6$ | 200 mL $min^{-1}$ | ≈500 | – | [100] |
| $La_{0.8}Zn_{0.2}MnO_3$ | 149 ppm *o*–Xylene | 200 mL $min^{-1}$ | ≈550 | – | [100] |
| $La_{1-x}Ce_xCoO_{3-\delta}$ | 500 ppm $C_6H_6$ | 90000 mL $g^{-1}$ $h^{-1}$ | 308 | – | [101] |
| $La_{0.9}Sr_{0.1}Mn_{0.9}Fe_{0.1}O_3$ | 500 ppm $C_7H_8$ | 30000 mL $g^{-1}$ $h^{-1}$ | 213 | 236 | [102] |
| $LaFe_{0.27}Mn_{0.73}O_3$ | 1000 ppm $C_7H_8$ | 40000 mL $g^{-1}$ $h^{-1}$ | – | <280 | [103] |
| $La0.8Ce_{0.2}Mn_{0.3}Fe_{0.7}O_3$ | 1000 ppm $C_7H_8$ | 6000 mL $g^{-1}$ $h^{-1}$ | 179 | 202 | [104] |
| $La_{0.8}Sr_{0.2}MnO_{3-\delta}$ | 0.6% $C_7H_8$ | 2000 mL $g^{-1}$ $h^{-1}$ | 260 | – | [105] |
| $LaNi_{0.5}Co_{0.5}O_{3-\delta}$ | 500 ppm $C_7H_8$ | 100 mL $min^{-1}$ | 221 | 239 | [106] |
| $La_{0.6}Ce_{0.4}Co_{0.6}Fe_{0.4}O_3$ | 1000 ppm $C_7H_8$ | 60000 mL $g^{-1}$ $h^{-1}$ | 190 | 318 | [107] |
| $La_{0.82}Sr_{0.18}CoO_3$ | 600 ppm $C_7H_8$ | 20000 mL $g^{-1}$ $h^{-1}$ | – | 210 | [108] |
| $Eu_{0.6}Sr_{0.4}FeO_3$ | 500 ppm $C_7H_8$ | 22500 mL $g^{-1}$ $h^{-1}$ | 279 | 305 | [109] |
| $La_{0.8}Cu_{0.2}MnO_3$ | 6000 ppm $C_7H_8$ | 5000 mL $g^{-1}$ $h^{-1}$ | – | – | [110] |
| $La_{0.8}Sr_{0.2}MnO_3$ | 6000 ppm $C_7H_8$ | 5000 mL $g^{-1}$ $h^{-1}$ | – | – | [110] |
| $La_{0.8}Sr_{0.2}CoO_3$ | 0.1 mol% $C_7H_8$ | 7200 mL $g^{-1}$ $h^{-1}$ | 163 | – | [111] |
| $LaMn_{0.5}Co_{0.5}O_3$ | 0.2 mol% $C_7H_8$ | 5000 mL $g^{-1}$ $h^{-1}$ | 200 | – | [112] |
| $LMNi_{4.50}$ | 900–1200 ppm $C_7H_8$ | 60000 mL $g^{-1}$ $h^{-1}$ | 234 | 278 | [113] |
| $La_{0.6}Sr_{0.4}CoO_{2.76}$ | 1000 ppm $C_7H_8$ | 20000 mL $g^{-1}$ $h^{-1}$ | – | >219 | [114] |
| $La_{0.5}S_{r0.5}MnO_{3-\delta}$ | 1000 ppm $C_7H_8$ | 20000 mL $g^{-1}$ $h^{-1}$ | 250 | 255 | [115] |
| $La_{0.6}Sr_{0.4}MnO_{3-\delta}$ | 1000 ppm $C_7H_8$ | 20000 mL $g^{-1}$ $h^{-1}$ | 299 | 310 | [115] |
| $La_{0.4}Sr_{0.6}MnO_{3-\delta}$ | 1000 ppm $C_7H_8$ | 20000 mL $g^{-1}$ $h^{-1}$ | 218 | 255 | [115] |
| $La_{0.5}Ca_{0.5}CoO_{3-\delta}$ | 2000 ppm $C_7H_8$ | 12000 mL $g^{-1}$ $h^{-1}$ | 183 | 218 | [116] |
| $La_{0.9}Ca_{0.1}CoO_3$ | 1000 ppm $C_7H_8$ | 60000 mL $g^{-1}$ $h^{-1}$ | – | 220 | [117] |
| Acid–etched $LaCoO_3$ | 1000 ppm $C_7H_8$ | 60000 mL $g^{-1}$ $h^{-1}$ | – | 215 | [117] |

(*Continued*)

**Table 2.** (Continued)

| Catalyst | Reactant composition | Space velocity/flow rate | $T_{50\%}$ [°C] | $T_{90\%}$ [°C] | References |
|---|---|---|---|---|---|
| $La_{0.99}Ag_{0.01}CoO_3$ | 1000 ppm $C_7H_8$ | 30000 mL $g^{-1}$ $h^{-1}$ | 275 | 300 | [118] |
| $La_{0.98}Ag_{0.02}CoO_3$ | 1000 ppm $C_7H_8$ | 30000 mL $g^{-1}$ $h^{-1}$ | 265 | 290 | [118] |
| $La_{0.97}Ag_{0.03}CoO_3$ | 1000 ppm $C_7H_8$ | 30000 mL $g^{-1}$ $h^{-1}$ | 249 | 284 | [118] |
| $La_{0.95}Ag_{0.05}CoO_3$ | 1000 ppm $C_7H_8$ | 30000 mL $g^{-1}$ $h^{-1}$ | 238 | 268 | [118] |
| $La_{0.75}Sr_{0.25}CoO_{3-\delta}$ | 500 ppm $C_7H_8$ | 30000 mL $g^{-1}$ $h^{-1}$ | 212 | – | [119] |

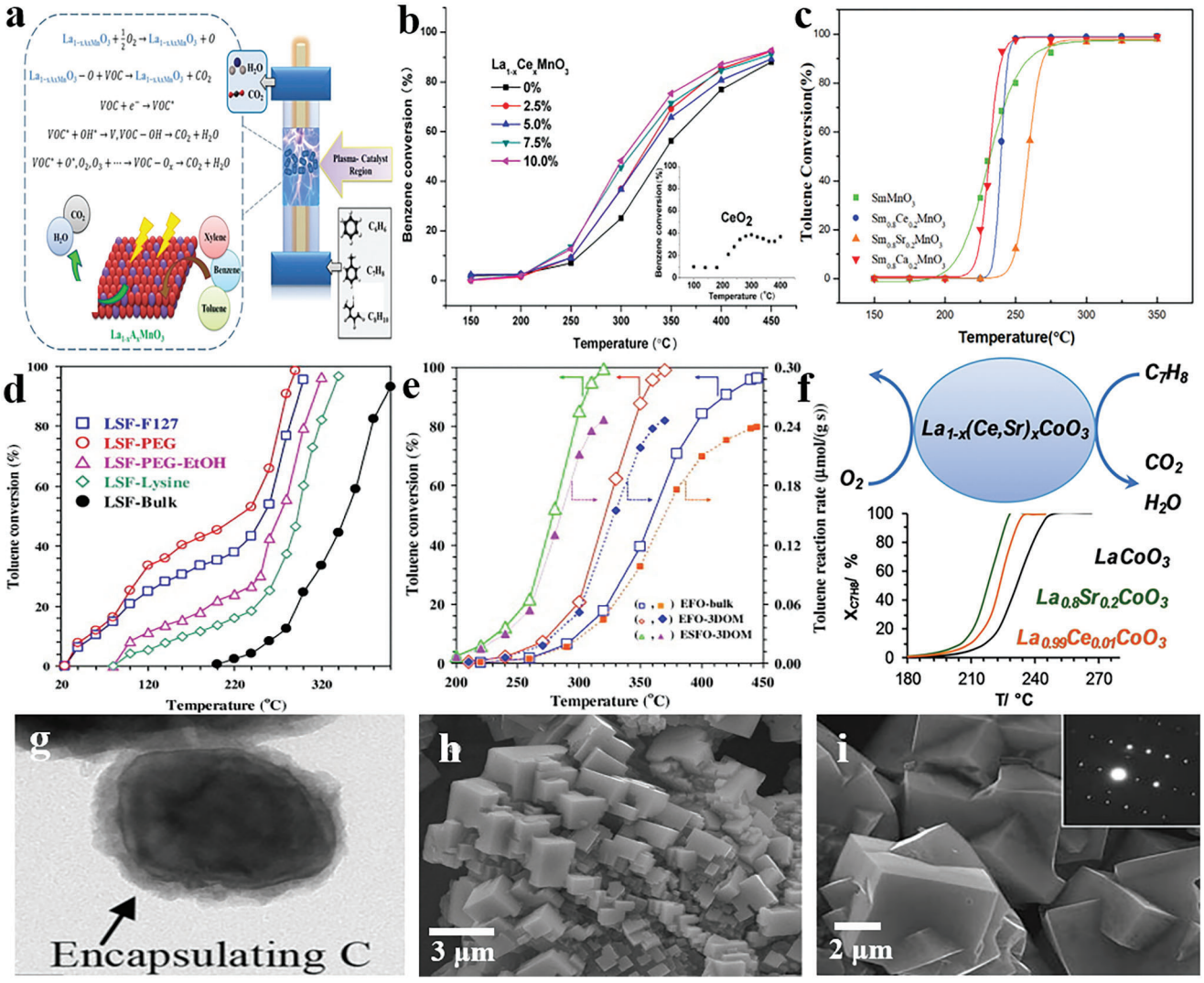


**Figure 2.** a) $La_{1-x}$ (Co, Zn, Mg, and Ba) $_xMnO_3$ for BTX degradation.[124] b) Benzene conversion of $La_{1-x}Ce_xMnO_3$. Reproduced with permission.[93] Copyright 2015, The Royal Society of Chemistry. c) Performance of $Sm_xA_{1-x}MnO_3$ (A = Ce, Sr, and Ca) perovskite for efficient catalytic oxidation of toluene.[94] d) Toluene conversion of the $La_{0.6}Sr_{0.4}FeO_{3-\delta}$ catalysts.[127] e) Toluene conversion and the corresponding reaction rate versus reaction temperature catalyzed by $Eu_{1-x}Sr_xFeO_3$–bulk, 3D ordered macroporous materials (3DOMs) $Eu_{1-x}Sr_xFeO_3$, and 3DOM $Eu_{1-x}Sr_xFeO_3$ catalysts.[125] f) La (Sr and Ce) $CoO_3$ and their properties in toluene catalytic total oxidation.[95] g) TEM image of used catalysts after steam reforming at 800 °C for 1 h.[74] h) SEM image of $La_{0.4}Sr_{0.6}MnO_{3-\delta}$.[128] i) SEM image and selected area electron diffraction patterns (inset) of $La_{0.6}Sr_{0.4}MnO_{3-\delta}$–270–50–0.35. Reproduced with permission.[129] Copyright 2013, Elsevier.

area, and promoting the exposure of active sites. This generated a large amount of lattice oxygen and more surface-adsorbed oxygen, resulting in a significant improvement in the catalytic activity. Zhao et al. prepared A–site substituted $La_{0.6}Sr_{0.4}FeO_{3-\delta}$, which showed excellent catalytic performance in toluene oxidation ($T_{10\%}$ = 54 °C, $T_{50\%}$ = 225 °C, and $T_{90\%}$ = 280 °C).[127] The high performance of the $La_{0.6}Sr_{0.4}FeO_{3-\delta}$ catalyst (Figure 2d) is related to its larger specific surface area. Inspired by this work, Ji et al. substituted $Sr^{2+}$ by $Eu^{2+}$ to afford $Eu_{1-x}Sr_xFeO_3$ (x = 0 and 0.4), which showed a greater surface oxygen concentration and remarkable activity in the oxidation of toluene (Figure 2e).[125] Heidinger et al. explored the oxidation of toluene with $Sr^{2+}$ and $Ce^{4+}$ substituted $LaCoO_3$.[95] The stability of the catalyst was improved, with substitution by $Sr^{2+}$ significantly altering the reduction and oxygen desorption properties of $Co^{3+}$, whereas substitution by $Ce^{4+}$ had only a limited effect (Figure 2f).

Soongprasit et al. synthesized $La_{1-x}Ce_xCoO_3$ (x = 0, 0.2, and 0.4) using a sol–gel method and found that $Ce^{4+}$ doping afforded filamentary carbon on the surface with Co located at the top of the carbon filament.[74] This structure was proposed to result in higher catalytic activity compared to the undoped catalyst (Figure 2g). A $La_{0.5}Sr_{0.5}MnO_{3-\delta}$ catalyst prepared by Deng et al. has a microcubic structure,[128] as shown in Figure 2h. Hydrothermally prepared $La_{0.6}Sr_{0.4}MnO_{3-\delta}$ for toluene oxidation, along with SEM and TEM image analysis of Sr–substituted $LaMnO_3$, revealed minimal morphological variation among catalysts.[129] The particles showed an interwoven microcubic shape, with $La_{0.6}Sr_{0.4}MnO_{3-\delta}$ exhibiting the highest catalytic activity (Figure 2i). Thus, elemental doping produces varying effects on the morphology and structure of the catalysts, which can affect the catalytic activity of $ABO_3$–PCs.

#### 4.2.2. B–Site Cation Doping

When the B–site ion of $ABO_3$–PCs is replaced by an ion of a different valency, it can cause lattice vacancies or a change in the valence state of the B–site ion, enabling the B–site ion a focal point for designing or improving $ABO_3$–PCs.[130] Transition metals such as Fe, Co, Ni, Mn and Cu can oxidize to unstable higher valence states, thereby altering catalytic activity. In addition, B–site substitution in $ABO_3$–PCs is more intricate compared to the A–site ions and warrants a thorough investigation. The catalytic activity of the $ABO_3$–PCs is determined by the nature of the excess metal cations at B site.[131] B–site transition metal ions exhibit a wide range of oxidation states, adding to the complexity of their substitution effects, surpassing those of the A–site ions.[132]

B–site doping in $ABO_3$–PCs has a profound effect on their catalytic properties and despite the complexity of synthesizing B–site doped materials,[133] it is an excellent approach to enhance catalyst performance. Hosseini et al. synthesized nanostructured $LaFeO_3$ and $LaZn_xFe_{1-x}O_3$ (x = 0.01, 0.05, 0.1, 0.2, and 0.3) perovskites and evaluated them in the catalytic oxidation of toluene (**Figure 3a**). Characterization data revealed that the total insertion of zinc into $LaFeO_3$ takes place when $x \leq 0.1$. However, ZnO segregation occurs to some extent, especially at $x > 0.1$. The catalytic activity increases with the zinc content, attributed in part to the presence of zinc oxide. The proportion of $LaZn_xFe_{1-x}O_3$ and zinc oxide influences the oxygen activation capacity and reactivity of the catalyst.[84] Lv et al. examined the catalytic performance of $LaCo_{1-x}M_xO_3$ (M = Fe, Cr, and Cu) under identical conditions and observed that introducing an appropriate proportion of specific metal cations at the B site of $ABO_3$–PCs could improve the catalytic activity, primarily through modifications in the oxidation state of the B site cations and oxygen vacancy content (Figure 3d,e).[79] Qi discovered that the doping of a small amount of $Co^{3+}$ at the B site of $LaNiO_3$ significantly enhances the catalytic oxidation of toluene,[96] while substituting $Ni^{3+}$ with $Cu^{2+}$ did not improve activity (Figure 3f,g). Among all the catalysts tested, $LaNi_{0.75}Co_{0.25}O_3$ exhibited the highest activity, achieving a relatively low temperature ($T_{90\%}$ = 225 °C) for toluene oxidation. Sahin et al. demonstrated that $LaMnO_3$ catalysts are more active than $LaFeO_3$ for toluene oxidation, with lower $T_{10\%}$, $T_{50\%}$, and $T_{90\%}$ values (Figure 3h).[70]

In addition to catalytic activity, B–site cations are also closely related to the durability of the perovskite and resistance to impurities (potential catalyst poisons). Vazquez et al. explored the effect of B–site cations in $SrTiO_3$ on catalytic behavior in toluene oxidation reactions (Figure 3b,c).[134] The addition of metal dopants ensured good stability over three catalytic cycles and lifetime tests. However, CuO deposition was observed on the surface of the Cu–doped catalyst. Incorporation of $Mn^{4+}$ into the $Ti^{4+}$ site in $SrTiO_3$ enhances the $O_{ads}/O_{latt}$ ratio and catalytic performance. Notably, $SrTi_{1-X}B_XO_3$ doped with $Mn^{4+}$ and $Cu^{2+}$ exhibited the highest catalytic activity for complete conversion of toluene to $CO_2$ at temperatures below 350 °C. Giraudon et al. loaded Pd NPs onto the surface of $ABO_3$–PCs using a hydrogen reduction calcination method and investigated the catalytic activity of $Pd/LaBO_3$ (B = Co, Fe, Mn, and Ni) in the oxidation of toluene, with the following trend observed: $Pd/LaFeO_3 > Pd/LaMnO_{3-\delta} > Pd/LaCoO_3 > Pd/LaNiO_3$.[135] The higher activity of $Pd/LaFeO_3$ for the total oxidation of toluene was attributed to a low amount of calcination and to the remarkable high stability of the perovskite lattice whatever the nature of the gas stream, which allowed the same palladium dispersion to be maintained at the different stages of the process and was stable under the oxidizing conditions. In contrast, phase transformations for the other perovskite lattices led to increases in the palladium particle size and was considered responsible for the lower activity (Figure 3i).

#### 4.2.3. A/B–Site Cation Doping

The A–site cations of $ABO_3$–PCs indirectly influence the valence state of the B–site ions and the oxygen vacancies within the catalyst, resulting in changes in the electronic state of the B–site ions and the B—O bond lengths,[136] with the B–site cations serving as the active catalytic centers in oxidation reactions.[137] In addition, the co-doping can realize the tuning of structural and electronic properties of $ABO_3$–PCs at the same time. Consequently, partial substitution of both A–site and B–site ions can be employed to improve the catalytic performance of $ABO_3$–PCs.[138]

Oskoui et al. used artificial neural networks to model the correlation between catalytic performance in toluene oxidation and catalytic parameters (the mole fraction of La, the mole fraction of Fe, calcination temperature (°C), and molar ratio of citric acid to the total nitrates in the precursor solution) using $La_xSr_{1-x}Fe_yCo_{1-y}O_3$ catalysts. They achieved 100% toluene

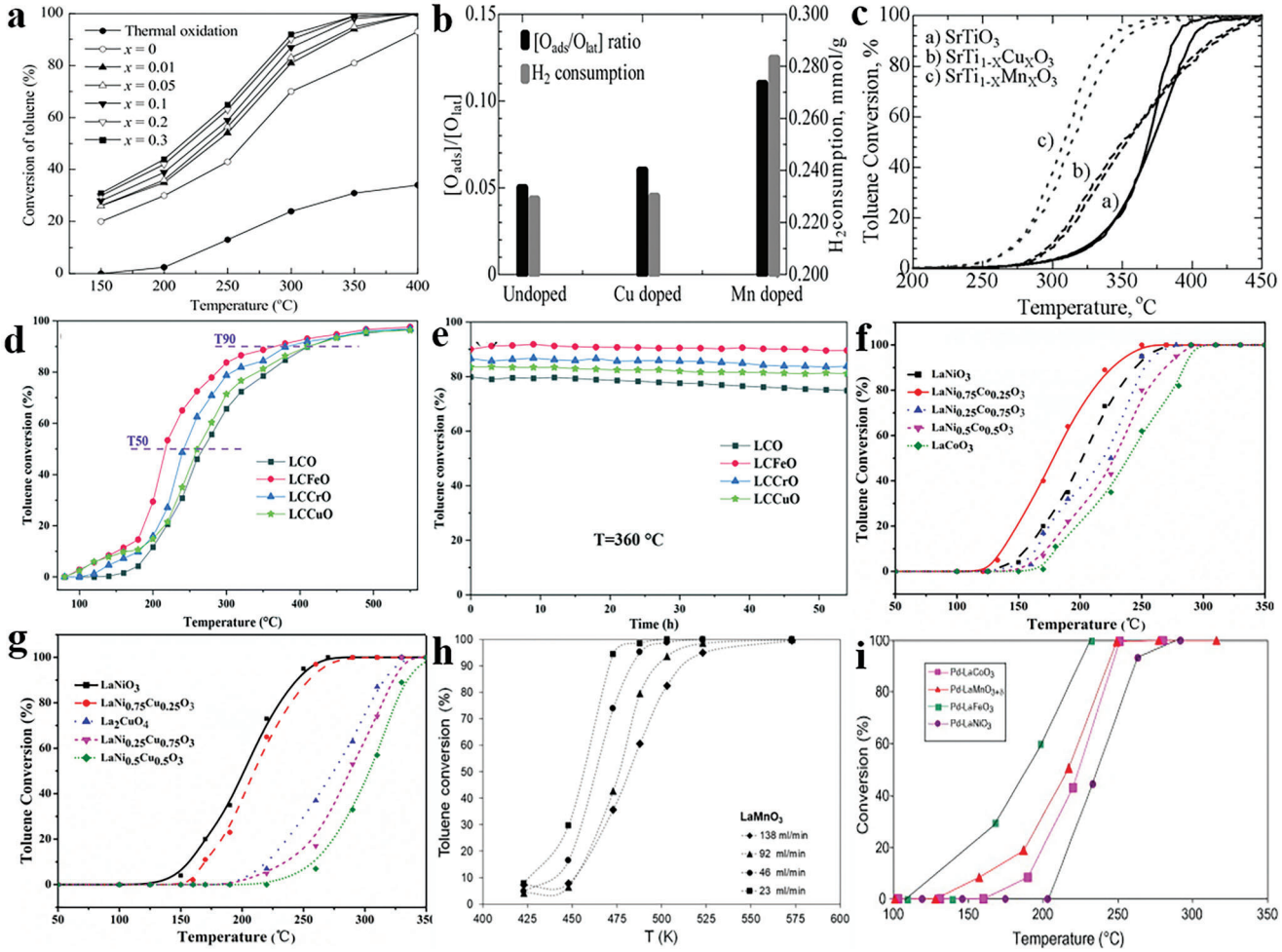


**Figure 3.** a) Performance of $LaMnO_3$ perovskites in the catalytic oxidation of toluene.[84] b,c) Catalytic oxidation of toluene using $SrTi_{1-X}B_XO_3$ (B = Cu and Mn). Reproduced with permission.[134] Copyright 2018, John Wiley and Sons. d,e) Catalytic performance of $LaCo_{1-x}M_xO_3$ (M = Fe, Cr, and Cu), $LaNi_xB_{1-x}O_3$ (B = Co and Cu).[79] f,g) $LaMnO_3$ (B = Co and Cu).[96] h) $LaMnO_3$.[70] i) $Pd/LaBO_3$ (B = Co, Fe, Mn, and Ni)[135] in the catalytic oxidation of toluene. Reproduced with permission.[135] Copyright 2007, Elsevier.

conversion for dual doped $La_{0.9}Sr_{0.1}Fe_{0.5}Co_{0.5}O_3$ at total conversion temperatures (Tc) = 700 and 800 °C, $La_{0.9}Sr_{0.1}Fe_{0.82}Co_{0.18}O_3$ at Tc = 700 °C, and $La_{0.8}Sr_{0.2}Fe_{0.66}Co_{0.34}O_3$ at Tc = 650 °C. A/B substitution strongly impacts on $La_xSr_{1-x}Fe_yCo_{1-y}O_3$ catalyst performance.[139] Li et al. employed an active milling method to prepare $La_{1-x}Sr_xCo_{1-y}Fe_yO_3$ perovskites and evaluate their catalytic properties in toluene oxidation (**Figure 4a**). $La_{0.5}Sr_{0.5}Co_{0.8}Fe_{0.2}O_{3-\delta}$ (LSCF) demonstrated remarkable catalytic activity with a $T_{90\%}$ of 270 °C (Figure 4b–c), attributed to improvements in redox ability through A/B site doping,[97] oxygen vacancy enrichment, and activation of lattice oxygen species. Yuan et al. investigated the impact of $Ce^{4+}$ and $Ni^{3+}$ doping in $La_{1-x}Ce_xMn_{1-y}Ni_yO_3$ perovskites on catalytic toluene oxidation, with $La_{0.8}Ce_{0.2}Mn_{0.8}Ni_{0.2}O_3$ exhibiting the highest conversion for toluene oxidation (Figure 4d,e).[98] XPS analysis revealed that $La_{0.8}Ce_{0.2}Mn_{0.8}Ni_{0.2}O_3$ possesses a higher lattice oxygen content and a lower redox onset temperature, both of which contribute to the catalytic oxidation of toluene (Figure 4f–h).

Co–doping is an efficient approach for generating active sites and enhancing the catalytic performance of $ABO_3$–PCs (see above). Moreover, several $ABO_3$–PCs with the composition $La_{1-x}Sr_xCo_{1-y}Fe_yO_3$ (x = 0 and 0.3; y = 0, 0.2, and 0.5) were prepared using a sol–gel method and their catalytic activity was studied in toluene oxidation.[99] Doping with $Sr^{2+}$ resulted in a flaccid morphology with reduced particle size and increased specific surface area. The study revealed that the catalytic activity was significantly increased with 30% $Sr^{2+}$ substituted in the A site, whereas a slight improvement was observed with 20% partial substitution of $Fe^{4+}$ at B site. Among the catalysts tested, $La_{0.7}Sr_{0.3}Co_{0.8}Fe_{0.2}O_3$ was the most active, attributed to the reduced particle size, increased specific surface area, the formation of $Fe^{4+}$ ions and the presence of electrophilic O–species, which serve as active sites that activate the substrate.

#### 4.2.4. $ABO_3$-PCs with Anion/Cation Defects

Due to the structural stability of $ABO_3$–PCs they can withstand the removal of ions to afford crystal defects that can be exploited as active sites in catalytic processes.[140] For example, Sun et al.

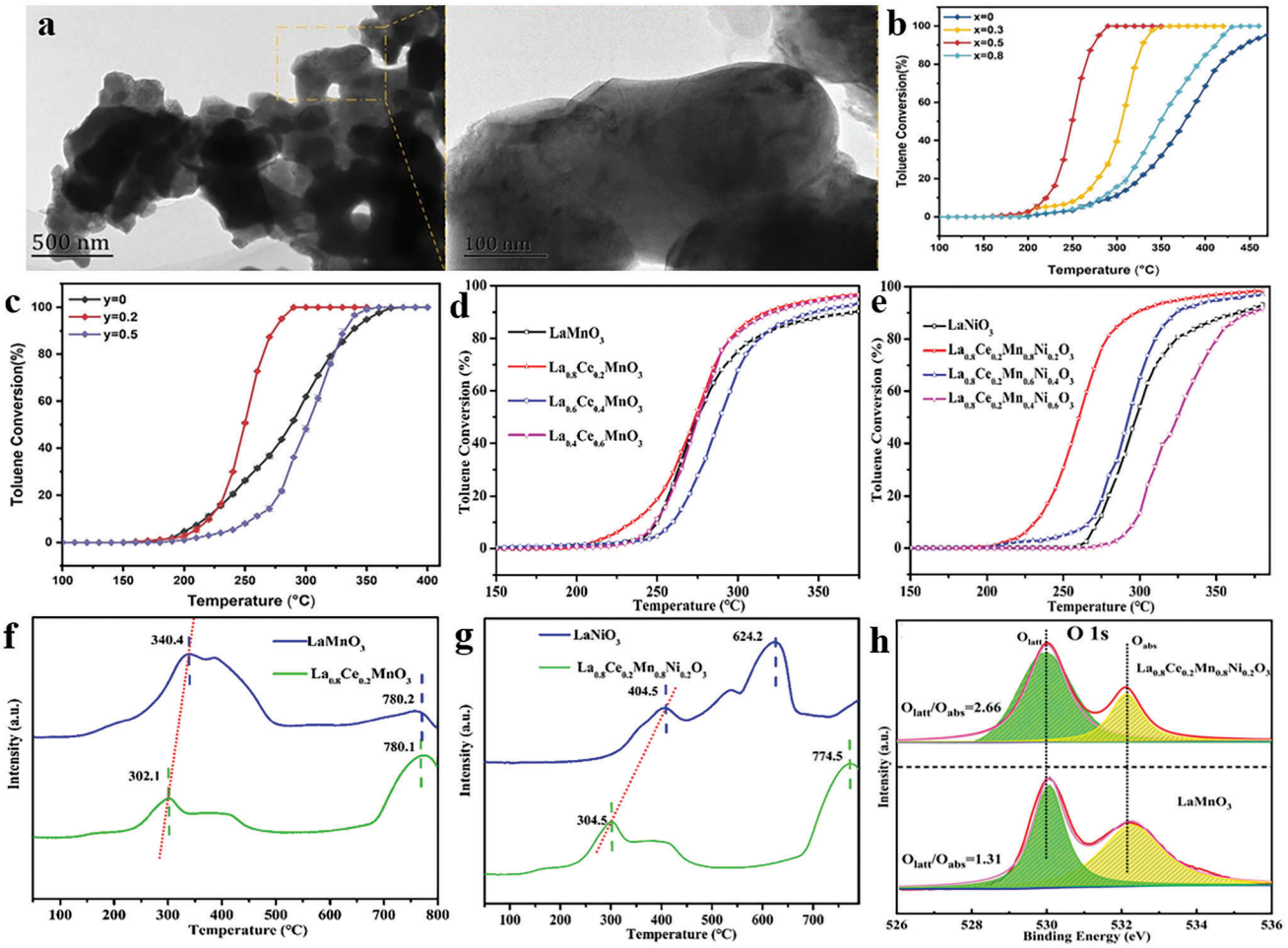


**Figure 4.** a) TEM of the LSCF catalyst. Toluene conversion using b) $La_{1-x}Sr_xCo_{0.8}Fe_{0.2}O_3$ (x = 0, 0.3, 0.5, and 0.8) and c) $La_{0.5}Sr_{0.5}Co_{1-y}Fe_y$ (y = 0, 0.2, and 0.5) catalysts. Reproduced with permission.[97] Copyright 2023, Elsevier. d) Catalytic activity of (d) $La_{1-x}Ce_xMnO_3$ perovskites (*x* = 0, 0.2, 0.4, and 0.6) and e) $LaNiO_3$, $La_{0.8}Ce_{0.2}Mn_{1-y}Ni_yO_3$ (*y* = 0, 0.2, 0.4, and 0.6). f) $H_2$–TPR of LMO and $La_{0.8}Ce_{0.2}MnO_3$, and g) $LaNiO_3$ and $La_{0.8}Ce_{0.2}Mn_{0.8}Ni_{0.2}O_3$. O 1s analysis of LMO and $La_{0.8}Ce_{0.2}Mn_{0.8}Ni_{0.2}O_3$. Reproduced with permission.[98] Copyright 2023, American Chemical Society.

doped $ABO_3$–PCs with $Ca^{2+}$ ions which leads to an increase in the number of oxygen vacancies and valency changes on the surface of the catalysts, resulting in a more active catalyst.[141] In addition, adjusting the ratio of A/B site cations can also promote the formation of oxygen vacancies on the surface to expose more active sites, e.g. Vincent et al. investigated the structure of $La_{0.8}MnO_{3-\delta}$, and found that varying the ratio of La/Mn affects the ratio of $Mn^{4+}/Mn^{3+}$ and generates vacancies.[142] Wu et al. synthesized a series of A–site cation-deficient $LaFeO_3$ PCs using the Pechini method, and evaluated them in the oxidation of toluene in the temperature range of 200–400 °C. Toluene conversion was maintained at 80% in a long cycle. Studies indicate that the introduction of A-site cation deficiencies affects the surface physicochemical properties of the PC, including enhanced oxygen vacancies, surface valence state, and surface oxygen content.[73] Indeed, Xu et al. designed a series of $La_{1-x}MnO_3$ and found that the $La^{3+}$ defects induce oxygen vacancies and adjust the electronic structure, significantly improving catalytic activity.[143]

An alternative way to generate defects is to dope the oxygen vacancies of $ABO_3$–PCs with $F^-$, $Cl^-$, $Br^-$, $S^{2-}$ etc., thus modifying the lattice structure, concentration of oxygen vacancies, specific surface area, etc., which in turn influences the electronic structure, oxygen diffusion properties, metal–oxygen bond strength, etc.[144] although further studies are required to fully understand these features.

### 4.3. Complexes Containing $ABO_3$ Compounds

#### *4.3.1. Noble Metal Composite $ABO_3$–PCs*

Incorporating noble metal NPs into $ABO_3$–PCs is an effective approach to improve their catalytic performance.[145] Dai et al. prepared $LaMnO_3$ and x$Au/LaMnO_3$ (x = 1.4, 3.1, and 4.9 wt.%) with chain–ordered macroporous structures, the latter with Au NPs dispersed on the surface.[146] Of the hybrid materials, 4.9$Au/LaMnO_3$ demonstrated the highest catalytic activity, achieving a $T_{50\%}$ and $T_{90\%}$ of 201 and 226 °C, respectively, for toluene oxidation. The high activity was attributed to high surface area and elevated $O_{ads}$ concentration, enhanced low–temperature

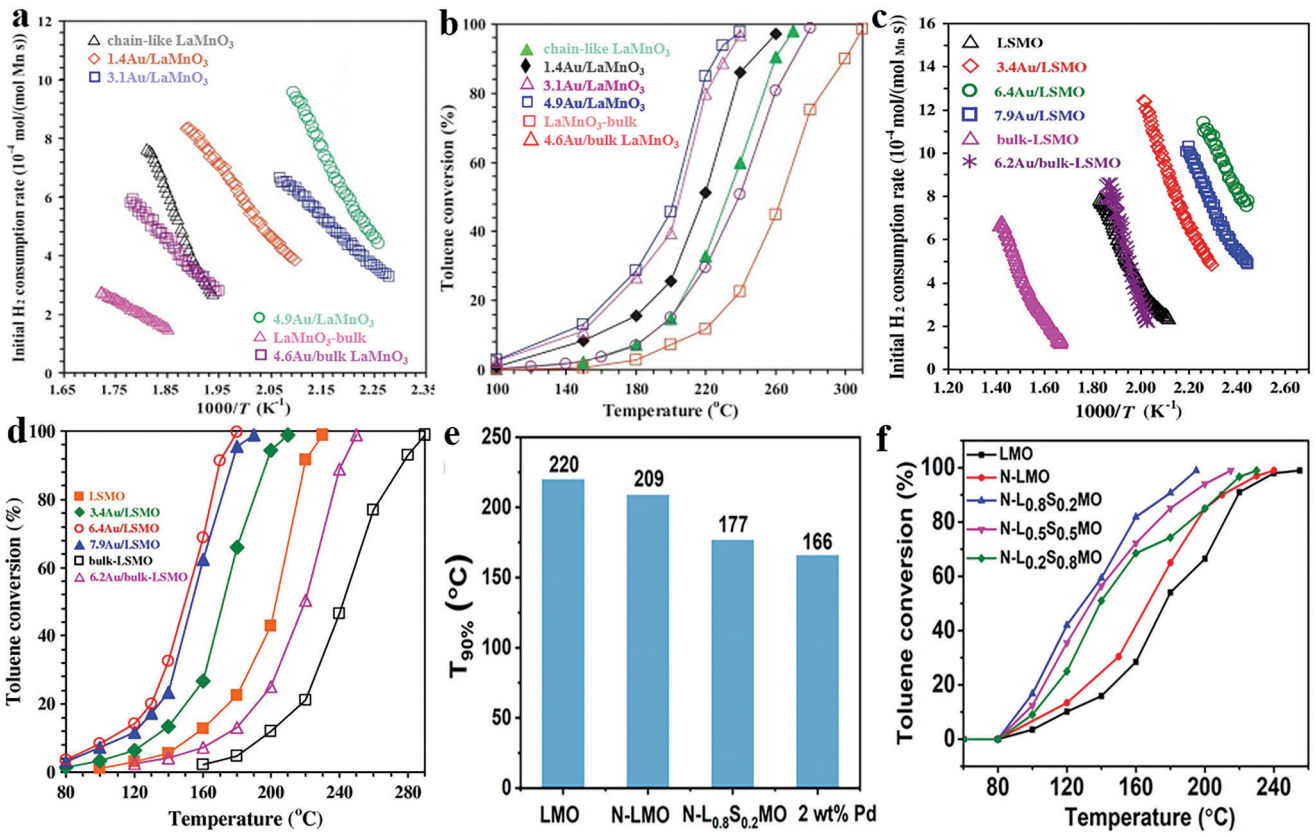


**Figure 5.** a) Initial $H_2$ consumption rate as a function of inverse temperature of chain–like $LaMnO_3$, 1.4Au/$LaMnO_3$, 3.1Au/$LaMnO_3$, 4.9Au/$LaMnO_3$, $LaMnO_3$–bulk, and 4.6Au/bulk $LaMnO_3$. b) Toluene conversion as a function of reaction temperature with the catalysts listed in (a).[146] c) Initial $H_2$ consumption rate as a function of inverse temperature of the LSMO and xAu/LSMO samples. d) Toluene conversion as a function of temperature with $La_{0.6}Sr_{0.4}MnO_3$ and xAu/LSMO catalysts.[147] e) The temperature difference of each catalyst when the toluene conversion rate reaches 90%. f) Toluene conversions as function of reaction temperature with $LaMnO_3$, N–LMO, N–$L_{0.8}S_{0.2}$MO, N–$L_{0.5}S_{0.5}$MO, and N–$L_{0.2}S_{0.8}$MO.[148] Copyright 2021, Elsevier.

reducibility, due to strong interactions between the Au NPs and $LaMnO_3$ support (**Figure 5**a,b). Similarly, Dai et al. fabricated 3DOM $La_{0.6}Sr_{0.4}MnO_3$ (LSMO) and its xAu/LSMO (x = 3.4–7.9 wt.%) catalysts.[147] They found that 6.4Au/LSMO exhibited the best catalytic activity, with $T_{50\%}$ and $T_{90\%}$ values for toluene oxidation at space velocity (SV) = 20000 mL $g^{-1}$ $h^{-1}$ reaching 150 and 170 °C, respectively (Figure 5c,d). The high activity was associated with a higher concentration of $O_{ads}$, improved low–temperature reducibility, and strong interaction between the Au NPs and LSMO.

Chen et al. used a nanocast array method to prepare Pd/$La_{0.8}Ce_{0.2}MnO_3$ catalysts, with optimal activity for the oxidation of toluene obtained using Pd/$La_{0.8}Ce_{0.2}MnO_3$/ZSM–5, attributed to higher acidity of the ZSM–5 support (Figure 5e,f). The Pd is highly dispersed on the surface of the $La_{0.8}Ce_{0.2}MnO_3$ perovskite, and the sample demonstrated a $T_{50\%}$ at 112 °C and $T_{90\%}$ at 227 °C for toluene oxidation.[148] Another related study using $ABO_3$–PC as a support material showed that it prevents Pd from sintering. Nishihata et al. reported the remarkable catalytic activity of Pd–$LaFeO_3$, which was attributed in part to the reversible movement of Pd in and out of the perovskite lattice under oxidizing and reducing atmospheres, respectively, effectively inhibiting the growth of Pd NPs. This finding was further confirmed in another study, stemming from the homogeneous distribution of Pd and the prevention of sintering. Consequently, Pd/$LaFeO_3$ exhibited a significantly higher catalytic activity in the oxidation of toluene compared to other composites.[135]

Liang et al. synthesized Ag/$LaCoO_3$ catalysts using an impregnation method,[118] and observed that the catalytic activity of Ag/LCO–250, Ag/LCO–450, and Ag/LCO–700 in toluene oxidation exceeded that of $LaCoO_3$. The enhanced catalytic performance was attributed to the interaction between the Ag/$Ag_2O$ and $LaCoO_3$ perovskite, as well as to differences in surface oxygen composition and reactivity. Li et al. prepared catalysts such as 3DOM $LaCoO_3$ and its xAu/3DOM $LaCoO_3$ (x = 0–7.63 wt.%) catalysts, finding that 7.63Au/3DOM $LaCoO_3$ displayed the most favorable catalytic performance for toluene oxidation. This PC benefited from a high surface area (24–29 $m^2$ $g^{-1}$), a high concentration of adsorbed oxygen species and optimal low–temperature oxidation.[149]

### *4.3.2. Metal Oxide Composite $ABO_3$–PCs*

The formation of chalcocite typically requires high calcination temperatures, which leads to a sacrifice of the specific surface area and therefore a lower number of active catalytic sites, typically reducing catalytic activity. It was found that loading

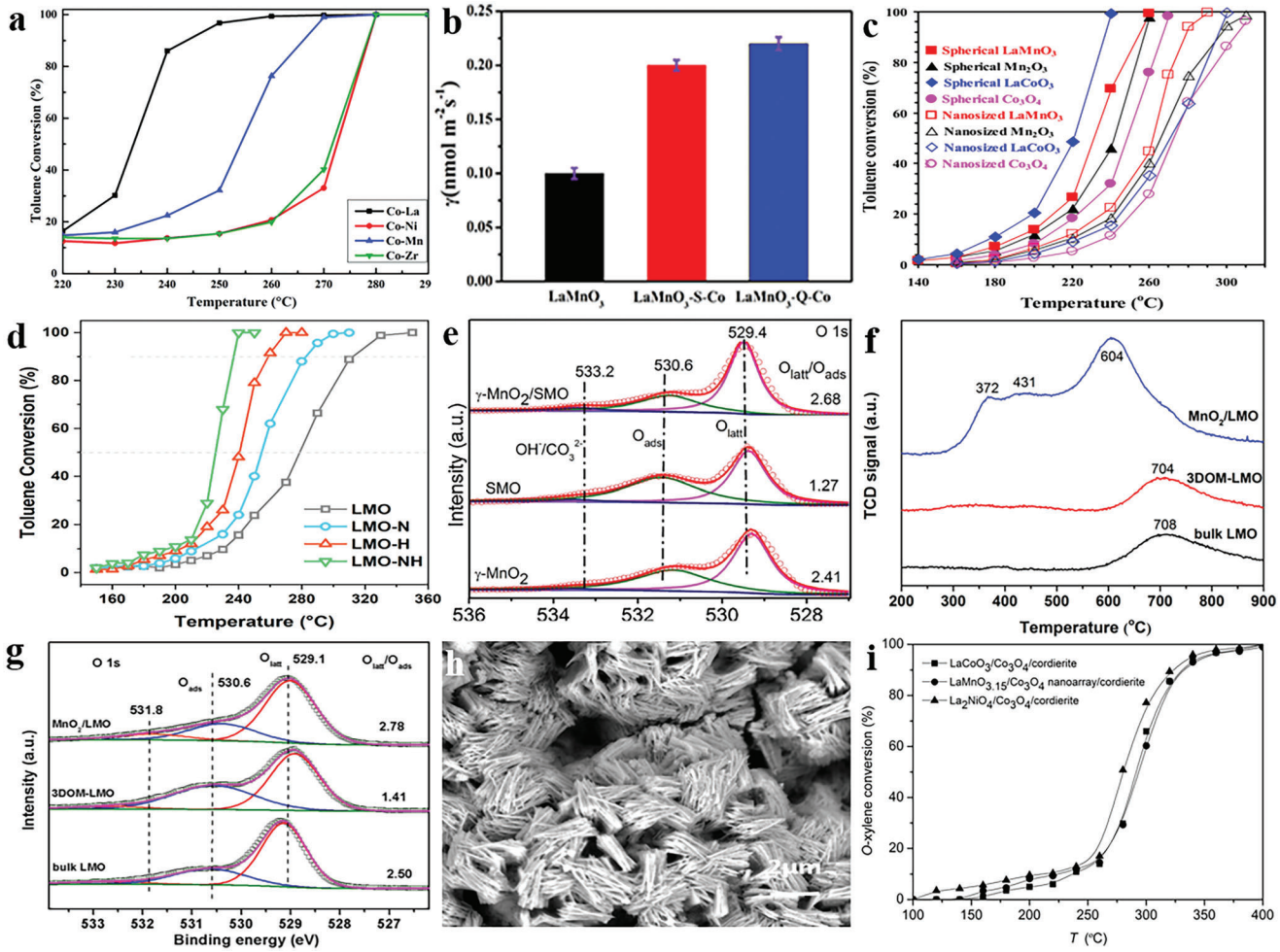


**Figure 6.** a) The effect of different metal oxides on the catalytic activity of $LaCo_xMn_{1-x}O_3$ in the oxidation of toluene. Reproduced with permission.[153] Copyright 2022, Elsevier. b) Toluene consumption rates at 250 °C and of different catalysts.[154] c) Catalytic oxidation activity of spherical and nano-sized $LaMO_3$ and MOx catalysts on toluene. Reproduced with permission.[155] Copyright 2013, American Chemical Society. d) Oxidation of toluene using $LaMnO_3$ catalysts.[156] e) O 1s XPS spectra of γ–$MnO_2$/SMO, SMO, and γ–$MnO_2$.[157] f) $O_2$–TPD profiles and g) O 1s XPS spectra of the $MnO_2$/LMO, 3DOM–LMO, and bulk LMO catalysts.[158] h) SEM image of $LaCoO_3/Co_3O_4$ nanowires. i) Oxidation of *o*–xylene catalyzed by $LaBO_3$ (B = Mn, Co, and Ni)/$Co_3O_4$/cordierite with different B types.[159]

$ABO_3$–PCs onto metal oxides is an effective approach for enhancing activity.[16] $Co_3O_4$ and $MnO_x$ are the most commonly used metal oxides combined with $ABO_3$–PCs.[150–152]

Wu et al. synthesized ultrafine $Co_3O_4$ decorated $Co_3O_4/LaCo_xMn_{1-x}O_3$, exhibiting significantly improved catalytic performance at a concentration of 1000 ppm and SV of 72000 mL $g^{-1}$ $h^{-1}$, resulting in a $T_{90\%}$ of 269 °C. The high catalytic activity may be attributed to the substantial surface area, abundant oxygen vacancies, and excellent reducibility (**Figure 6a**). Moreover, density functional theory calculations revealed that $Co_3O_4$ doping and interfacial effects of $Co_3O_4/LaCo_xMn_{1-x}O_3$ result in lower activation energies for C–H cleavage.[153] In another study by Zhang et al., $Co_3O_4$ catalysts were modified with different metals M (M = La, Mn, Zr, and Ni) for the catalytic oxidation of toluene. They found that $Co_3O_4$–$LaCoO_3$ exhibited excellent catalytic performance with a $T_{90\%}$ of 243 °C and higher conversion rate (Figure 6b). Analysis suggests that the excellent activity of $Co_3O_4$–$LaCoO_3$ may be attributed to its high specific surface area with many $Co^{3+}$ species and abundant adsorbed oxygen species.[154] Dai et al. also discovered that hollow spherical $LaCoO_3$ and solid spherical $Co_3O_4$ outperformed their nano–sized counterparts in toluene oxidation.[155] Their outstanding catalytic properties were attributed to their large surface area, high oxygen adsorption concentration, and better low–temperature oxidation (Figure 6c).

Wang et al. obtained a $MnO_2$/LMO material with a rod–like morphology through an alkaline hydrothermal treatment with acid etching (Figure 6d), with the material catalyzing the oxidation of toluene with a $T_{90\%}$ of 236 °C.[156] Compared with bulk LMO, LMO with an alkaline hydrothermal treatment (LMO–N) and LMO with an acid treatment (LMO–H), LMO with an alkaline hydrothermal treatment with acid etching (LMO–NH) has a higher ratio of $Mn^{4+}/Mn^{3+}$ ions on the surface, which significantly improves the low–temperature catalytic activity by lowering the apparent activation energy (< 38.6 kJ $mol^{-1}$) of the reaction. LMO–NH also has a high lattice oxygen

concentration and surface oxygen vacancy density, thus accelerating the adsorption and reaction of toluene. In another study, $\gamma$–$MnO_2$, $SmMnO_3$, and $\gamma$–$MnO_2$/$SmMnO_3$ were synthesized, and compared with $\gamma$–$MnO_2$/$SmMnO_3$ formed from the situ growth of $\gamma$–$MnO_2$ on the surface of $SmMnO_3$. Of the three materials, $\gamma$–$MnO_2$/$SmMnO_3$ was found to have the highest activity in BTX oxidation in wet air (10 vol.%), attributed to a higher molar ratio of surface lattice oxygen to adsorbed oxygen ($O_{latt}/O_{ads}$) (Figure 6e) and improved low–temperature processing.[157] Li et al. reported $MnO_2$/$LaMnO_3$, which at 290 °C could completely oxidize toluene to $CO_2$ and $H_2O$, with a toluene/oxygen molar ratio of 1/100 and a space velocity of 120000 mL $g^{-1}$ $h^{-1}$. Based on $O_2$–TPD and O 1s XPS data (Figure 6f,g), it was found that the catalyst has abundant oxygen species and high lattice oxygen mobility.[158]

$ABO_3$–PCs have also been immobilized on a range of materials. Sun et al. successfully integrated different perovskite/hybrid perovskites onto the surface of cordierite honeycomb ceramics and evaluated them in the catalytic oxidation of xylene. The $La_2NiO_4/Co_3O_4$ composite exhibited a unique 3DOM hierarchical hollow microsphere structure composed of nanowires (Figure 6h). Compared with $LaCoO_3$/cordierite, $Co_3O_4$/cordierite, $LaMnO_{3.15}/Co_3O_4$/cordierite and $LaCoO_3/Co_3O_4$/cordierite, the $La_2NiO_4/Co_3O_4$/cordierite catalyst displayed superior catalytic performance, achieving a $T_{90\%}$ for *o*–xylene of 299 °C (Figure 6i). The high catalytic activity of $La_2NiO_4/Co_3O_4$/cordierite catalysts was attributed to the high specific surface area, large oxygen storage capacity, and synergistic effects between $La_2NiO_4$ and $Co_3O_4$.[159]

#### 4.3.3. Other Composite $ABO_3$–PCs

$ABO_3$–PCs are often limited by their low specific surface areas and low mechanical strength, which impacts on their activity and lifetime. Incorporating dispersed $ABO_3$–PCs on or within a support material can overcome these limitations. Various support materials have been evaluated including $Al_2O_3$, $CeO_2$, MgO, $MnO_2$, and $ZrO_2$.

Si et al. reported that 3DOM $LaMnO_3$ dispersed and immobilized on $MnO_2$ results in better catalytic performance in the oxidation of toluene compared to the unsupported catalyst.[158] Similarly, Wang et al. found that $La_{0.8}Ce_{0.2}MnO_3/CeO_2$ nanocubes exhibit high catalytic efficiency in the oxidation of toluene due to having a high specific surface area, more oxygen vacancies, better low–temperature reduction, and highly active oxygen species.[160] Composite catalysts have also shown promising results, as demonstrated by Alifantim et al., who immobilized 10–20 wt.% $LaCoO_3$ on $Ce_{1-x}Zr_xO_2$ (x = 0–0.3) and observed significant activity in the oxidation of benzene and toluene in the temperature range 100–500 °C. In contrast, bulk $LaCoO_3$ catalysts were less active and required higher temperatures.[161] Giroir–Fendler et al. drew similar conclusions, highlighting the influence of the interaction between $LaMnO_3$ and the substrate on oxygen diffusion and catalytic performance in toluene oxidation.[62] Xue et al. supported $La_{0.8}Sr_{0.2}MnO_3$ and $La_{0.8}Sr_{0.2}CoO_3$ on $\gamma$–$Al_2O_3$ via an impregnation method, with the catalysts achieving 90% xylene conversion at 260 °C.[162]

**Table 3** summarizes the $ABO_3$–PCs immobilized on various support materials and their performance in the catalytic oxidation of BTX. In general, the immobilized catalysts exhibit superior oxygen exchange capacity and catalytic activity compared to dispersed $ABO_3$–PCs. Furthermore, certain supports compensate for the surface properties lacking in $ABO_3$, thereby enhancing catalytic activity. The morphology, crystallinity, reducibility, acidity, hydrophobicity, and other physicochemical properties of the support affect catalytic activity. For example, a hydrophobic surface repels water and favors interactions with hydrophobic BTX leading to improved catalytic performance.[153]

## 5. Factors Affecting Catalytic Activity

### 5.1. Effect of Morphology

Controlling and optimizing the morphology of $ABO_3$–PCs is important due to the impact that catalyst morphology has on performance, and the route used to prepare $ABO_3$–PCs plays a key role in governing their morphology.[183] Currently, the main approaches used to modulate the morphology $ABO_3$–PCs involves utilizing templates with high specific surface areas and well–defined channel structures in their synthesis. For example, Chen et al. fabricated catalysts comprising Pd supported on $La_{1-x}Sr_xMnO_3$ mesoporous nanotube arrays using SBA-15 as a hard template (**Figure 7a**). The morphological control results in catalysts with a very high specific surface area, ordered hollow orifices, and large pore size. Notably, compared to $La_{0.8}Sr_{0.2}MnO_3$, the 2 wt.% $Pd@La_{0.8}Sr_{0.2}MnO_3$ catalyst exhibits outstanding catalytic performance in the oxidation of toluene ($T_{90\%}$ = 177 °C) and shows excellent stability. Such improved catalytic activity can primarily be attributed to the high surface area, high $Mn^{4+}/Mn^{3+}$ ratio, and abundant lattice oxygens exhibits outstanding catalytic performance in the oxidation of toluene and shows excellent stability.[148]

Hydrothermal methods, melt polymerization and template methods have been employed to modulate the morphology of $ABO_3$–PCs.[184,185] Liu et al. proposed an industrially scalable one–step melt polymerization strategy to prepare $SmMnO_3$ with distinct morphological structures.[186] Through citric acid polymerization (Figure 7b), they were able to produce $SmMnO_3$ with three different morphologies, i.e. reticular, granular, and bulk. Among these catalysts, reticular $SmMnO_3$ with a porous structure (Figure 7f,g) showed the highest activity, being able to completely oxidize toluene, benzene, and *o*–xylene at 240, 270, and 300 °C, respectively. Benzene and *o*–xylene were completely converted into carbon dioxide and water at these temperatures, demonstrating comparable activity to noble metal catalysts. The remarkable catalytic efficiency of reticulated $SmMnO_3$ for BTX was attributed to its distinctive structure, high surface $Mn^{4+}/Mn^{3+}$ ratio, and $O_{latt}/O_{ads}$ composition and strong reduction properties. In another study conducted by Deng et al., single–crystal microcubic $La_{0.5}Sr_{0.5}MnO_{3-\delta}$ was prepared by a hydrothermal method (Figure 7c). The temperature used was found to have a significant effect on the morphology and properties of the $La_{0.5}Sr_{0.5}MnO_{3-\delta}$ catalyst. The catalysts hydrothermally treated at 250 °C showed the optimal activity in toluene oxidation, attributed to surface Mn enrichment, a high $Mn^{4+}/Mn^{3+}$ ratio, and extensive surface oxygen vacancies provided by the

**Table 3.** Composite and immobilized $ABO_3$–PCs evaluated in the catalytic oxidation of BTX.

| Catalyst | Reactant composition | Space velocity/flow rate | $T_{50\%}$ [°C] | $T_{90\%}$ [°C] | References |
|---|---|---|---|---|---|
| Mn–$LaNiO_3$ | 400 ppm $C_6H_6$ | 200 mL $min^{-1}$ | ≈280 | – | [67] |
| $LaCoO_3$/MgO | 500 ppm $C_7H_8$ | 192000 mL $g^{-1}$ $h^{-1}$ | – | 248 | [69] |
| $La_{0.9}Ca_{0.1}CoO_3$/MgO | 500 ppm $C_7H_8$ | 192000 mL $g^{-1}$ $h^{-1}$ | 214 | 228 | [69] |
| $LaMnO_3$/$LaMn_2O_5$ | 210 ppm $C_7H_8$ | 138 mL $min^{-1}$ | 481 | 515 | [70] |
| $La_{0.75}Ag_{0.25}MnO_3$ | 5 g $m^{-3}$ $C_7H_8$ | 18000 mL $g^{-1}$ $h^{-1}$ | 140 | 230 | [78] |
| $LaMnO_3$/0.5% Pt | 5 g $m^{-3}$ $C_7H_8$ | 18000 mL $g^{-1}$ $h^{-1}$ | 160 | 220 | [78] |
| $LaMnO_3$/0.2% Pt | 5 g $m^{-3}$ $C_7H_8$ | 18000 mL $g^{-1}$ $h^{-1}$ | 170 | 230 | [78] |
| $LaMnO_3$/0.1% Pt | 5 g $m^{-3}$ $C_7H_8$ | 18000 mL $g^{-1}$ $h^{-1}$ | 170 | 230 | [78] |
| $LaMnO_3$/0.02% Pt | 5 g $m^{-3}$ $C_7H_8$ | 18000 mL $g^{-1}$ $h^{-1}$ | 165 | 230 | [78] |
| $LaMnO_3$/0.5% Pd | 5 g $m^{-3}$ $C_7H_8$ | 18000 mL $g^{-1}$ $h^{-1}$ | 175 | 250 | [78] |
| $LaMnO_3$/0.1% Pd | 5 g $m^{-3}$ $C_7H_8$ | 18000 mL $g^{-1}$ $h^{-1}$ | 165 | 260 | [78] |
| 5 wt.%$MnO_x$/3DOM $LaMnO_3$ | 1000 ppm $C_7H_8$ | 20000 mL $g^{-1}$ $h^{-1}$ | 210 | 228 | [80] |
| 8 wt.%MnOx/3DOM $LaMnO_3$ | 1000 ppm $C_7H_8$ | 20000 mL $g^{-1}$ $h^{-1}$ | 208 | 225 | [80] |
| 12 wt.%$MnO_x$/3DOM $LaMnO_3$ | 1000 ppm $C_7H_8$ | 20000 mL $g^{-1}$ $h^{-1}$ | 203 | 222 | [80] |
| 16 wt.%MnOx/3DOM $LaMnO_3$ | 1000 ppm $C_7H_8$ | 20000 mL $g^{-1}$ $h^{-1}$ | 193 | 215 | [80] |
| $MnO_2$/$LaMnO_3$ | 1000 ppm $C_7H_8$ | 40000 mL $g^{-1}$ $h^{-1}$ | 225 | 234 | [83] |
| $LaMnO_3$/$TiO_2$ | 1000 ppm $C_7H_8$ | 100 mL $min^{-1}$ | 278 | 303 | [86] |
| Pd/ $LaCoO_3$ | 1800 ppm $C_7H_8$ | 3000 mL $g^{-1}$ $h^{-1}$ | 223 | – | [135] |
| Pd/$LaFeO_3$ | 1800 ppm $C_7H_8$ | 3000 mL $g^{-1}$ $h^{-1}$ | 185 | – | [135] |
| Pd/$LaMnO_{3-\delta}$ | 1800 ppm $C_7H_8$ | 3000 mL $g^{-1}$ $h^{-1}$ | 217 | – | [135] |
| Pd/$LaNiO_3$ | 1800 ppm $C_7H_8$ | 3000 mL $g^{-1}$ $h^{-1}$ | 234 | – | [135] |
| Au/$LaMnO_3$ | 1000 ppm $C_7H_8$ | 20000 mL $g^{-1}$ $h^{-1}$ | 201 | 226 | [146] |
| Pd–$La_{0.8}Sr_{0.2}MnO_3$ | 50 ppm $C_7H_8$ | 36000 mL $g^{-1}$ $h^{-1}$ | – | 166 | [148] |
| Au/3DOM $LaCoO_3$ | 1000 ppm $C_7H_8$ | 20000 mL $g^{-1}$ $h^{-1}$ | 188 | 202 | [149] |
| $Co_3O_4$/$LaCoO_3$ | 500 ppm | 100 mL $min^{-1}$ | – | 243 | [154] |
| Co–$LaMnO_3$ | 1000 ppm $C_7H_8$ | 72000 mL $g^{-1}$ $h^{-1}$ | – | 269 | [153] |
| $\gamma$–$MnO_2$/$SmMnO_3$ | 1000 ppm *o*–Xylene | 60000 mL $g^{-1}$ $h^{-1}$ | 232 | 250 | [157] |
| $LaMnO_{3.15}$/$Co_3O_4$/cordierite | *o*–Xylene | – | – | 330 | [159] |
| $LaCoO_3$/$Co_3O_4$/cordierite | *o*–Xylene | – | – | 331 | [159] |
| $La_2NiO_4$/$Co_3O_4$/cordierite | *o*–Xylene | – | – | 320 | [159] |
| $La_{0.8}Ce_{0.2}MnO_3$/$CeO_2$ | 300 ppm $C_7H_8$ | 12000 mL $g^{-1}$ $h^{-1}$ | – | <240 | [160] |
| Pd–$CeMnO_3$ | 500 ppm $C_6H_6$ | 20000 mL $g^{-1}$ $h^{-1}$ | 139 | 186 | [163] |
| Pd–$CeMnO_3$ | 500 ppm $C_7H_8$ | 20000 mL $g^{-1}$ $h^{-1}$ | 145 | 186 | [67] |
| Pd–$CeMnO_3$ | 500 ppm $C_6H_6$ | 19200 mL $g^{-1}$ $h^{-1}$ | 139 | 184 | [164] |
| $CeO_2$/$LaCoO_3$ | 500 ppm $C_6H_6$ | 80 mL $min^{-1}$ | 288 | – | [165] |
| Bulk $SmMnO_3$ | 12000 ppm $C_6H_6$ | 100 mL $min^{-1}$ | 237 | 275 | [166] |
| $\gamma$–$MnO_2$/$SmMnO_3$ | 1000 ppm $C_6H_6$ | 60000 mL $g^{-1}$ $h^{-1}$ | 213 | 226 | [166] |
| $\gamma$–$MnO_2$/$SmMnO_3$ | 1000 ppm $C_7H_8$ | 60000 mL $g^{-1}$ $h^{-1}$ | 187 | 208 | [166] |
| CuO/$Zr_xCe_{1-x}Oy$ | 1000 ppm $C_6H_6$ | 96000 mL $g^{-1}$ $h^{-1}$ | – | <300 | [167] |
| Cordierite–$NiMnO_3$ | 1000 ppm $C_6H_6$ | 15000 mL $g^{-1}$ $h^{-1}$ | – | 275 | [168] |
| Pd–$LaCoO_3$–cordierite | 1500 ppm $C_6H_6$ | 20000 mL $g^{-1}$ $h^{-1}$ | ≈280 | – | [169] |
| Cu– $LaCoO_3$–cordierite | 1500 ppm $C_6H_6$ | 20000 mL $g^{-1}$ $h^{-1}$ | ≈300 | – | [169] |
| Ceria–based–$LaCoO_3$ | 1700 ppm $C_6H_6$ | 60000 mL $g^{-1}$ $h^{-1}$ | 330 | – | [170] |
| Ceria–based–$LaCoO_3$ | 1700 ppm $C_6H_6$ | 60000 mL $g^{-1}$ $h^{-1}$ | 244 | – | [170] |
| $SmMnO_3$/ cordierite | 1000 ppm $C_6H_6$ | 20000 mL $g^{-1}$ $h^{-1}$ | ≈285 | ≈345 | [171] |
| $\gamma$–$MnO_2$/$SmMnO_3$ | 1000 ppm $C_7H_8$ | 60000 mL $g^{-1}$ $h^{-1}$ | 187 | 208 | [171] |
| $\gamma$–$MnO_2$/$SmMnO_3$ | 1000 ppm *o*–Xylene | 60000 mL $g^{-1}$ $h^{-1}$ | 232 | 250 | [171] |
| $LaMnO_3$/$\delta$–$MnO_2$ | 1000 ppm $C_7H_8$ | 30000 mL $g^{-1}$ $h^{-1}$ | – | 258 | [172] |
| Pd/$La_{0.8}Ce_{0.2}MnO_3$/ZSM–5 | 3 mg $L^{-1}$ $C_7H_8$ | 20000 mL $g^{-1}$ $h^{-1}$ | – | 285 | [173] |
| $La_{0.75}Ce_{0.25}MnO_3$/$CeO_2$ | 1000 ppm $C_7H_8$ | 18000 mL $g^{-1}$ $h^{-1}$ | – | 250 | [174] |

(*Continued*)

**Table 3.** (Continued)

| Catalyst | Reactant composition | Space velocity/flow rate | $T_{50\%}$ [°C] | $T_{90\%}$ [°C] | References |
|---|---|---|---|---|---|
| $LaCoO_3/ZrO_2$/cordierite | 1000 ppm $C_7H_8$ | 100 mL $min^{-1}$ | 159 | 216 | [175] |
| $LaCoO_3/r–Al_2O_3$/cordierite | 1000 ppm $C_7H_8$ | 100 mL $min^{-1}$ | 180 | 220 | [175] |
| $LaCoO_3/TiO_2$/cordierite | 1000 ppm $C_7H_8$ | 100 mL $min^{-1}$ | 206 | 233 | [175] |
| $LaCoO_3$ /cordierite | 1000 ppm $C_7H_8$ | 100 mL $min^{-1}$ | 210 | 240 | [175] |
| $Mn_3O_4$–Au 3DOM $La_{0.6}Sr_{0.4}CoO_3$ | 1000 ppm $C_7H_8$ | 20000 mL $g^{-1}$ $h^{-1}$ | 214 | 230 | [176] |
| Au/$MnO_x$/$La_{0.6}Sr_{0.4}MnO_3$ 3DOM | 1000 ppm $C_7H_8$ | 20000 mL $g^{-1}$ $h^{-1}$ | 205 | 220 | [177] |
| 80Co–20La | 500 ppm $C_7H_8$ | 100 mL $min^{-1}$ | 230 | 242 | [178] |
| $LaCoO_3$/SBA–15 | 1000 ppm $C_7H_8$ | 20000 mL $g^{-1}$ $h^{-1}$ | 284 | 320 | [179] |
| $EuCoO_3/LaCoO_3$ | 1700 ppm $C_7H_8$ | 100 mL $min^{-1}$ | 256 | – | [180] |
| Fe doped $LaMnO_3/Al_2O_3$ | 200 ppm *o*–Xylene | 200 mL $min^{-1}$ | 744 J/L | – | [181] |
| $SmMnO_3/SmMn_2O_5$ | 1000 ppm *o*–Xylene | 100 mL $min^{-1}$ | – | 280 | [182] |

microcubic structure.[128] Wang et al. developed a molten salt route to control the morphology of porous $LaMnO_3$ NPs, i.e. spherical and cubic, using porous $Mn_2O_3$ spheres as a template (Figure 7d,e). These catalysts exhibit high catalytic performance in the oxidation of toluene, with the cubic structure having the highest activity. The $T_{10\%}$, $T_{50\%}$ and $T_{90\%}$ temperatures for toluene oxidation in the presence of cubic $LaMnO_3$ are 110, 170, and 220 °C, respectively, at a toluene/oxygen molar ratio = 1/400 and SV = 20000 mL $g^{-1}$ $h^{-1}$. It was inferred that the high surface $Mn^{4+}/Mn^{3+}$ molar ratio and facile low–temperature oxidation of cubic $LaMnO_3$ enhance the catalytic performance.[187] Rahemi et al. synthesized $La_{0.8}Zn_{0.2}MnO_3$ using a sol–gel method with different citric acid to metal nitrate ratios with lanthanum, manganese, and zinc (La/Zn/Mn molar ratio of 0.8/0.2/1). With the increase of calcination temperature, $La_{0.8}Zn_{0.2}MnO_3$ shows a spongy porous structure (Figure 7h), attributed to the large amount of gas generated during the calcination process. At a calcination temperature of 550 °C the particles vary in size and shape and are aggregated, whereas at calcination temperatures of 600 and 650 °C spherical NPs are formed. At a calcination temperature of 700 °C the particles are spherical and dispersed, which facilitates mass transfer to enhance the activity of the catalyst.[100]

### 5.2. The Impact of Structural Regulation

Nano–structuring, such as building 3DOM or core–shell structures can generate $ABO_3$–PCs with large specific surface areas and stabilities that are conducive to high catalytic performance. **Table 4** summarizes catalyst structures and how structure influences the catalytic oxidation of benzene and toluene. Hollow multishell structures are particularly active catalysts for the oxidation of BTX due to their porous nature and mutual interactions between different shells. This arrangement results in a relatively large effective speciated surface area with excellent resistance to sintering. For example, Chen et al. synthesized spherical $PrMnO_3$ hollow multishells ($PrMnO_3$–HoMSs) and evaluated them as catalysts in the oxidation of toluene (**Figure 8a,b**). Compared with the catalysts ($PrMnO_3$–PC) synthesized by a co–precipitation method, $PrMnO_3$–HoMSs exhibit higher catalytic performance in toluene oxidation. The activity was attributed to the high specific surface area of the porous, polycrystalline structure, and an abundance of reactive oxygen species.[188]

3DOM structures have high porosities characterized by tunable pore sizes (> 50 nm) and a regular, uniform arrangement of pores that allows for tight pore connectivity and high porosity. Such structures facilitate gas diffusion and enhances contact efficiency during the catalytic BTX oxidation treatment, resulting in significantly improved gas diffusion efficiency. Zhao et al. synthesized cordierite–supported 3DOM $La_{0.8}Ce_{0.2}MnO_3$ (Figure 8c,d) using a PMMA template method. The catalysts calcined at 600 °C show optimal performance ($T_{50\%}$ = 147 °C; $T_{90\%}$ = 217 °C; Ea = 27.01 kJ $mol^{-1}$; SV = 6000 mL $g^{-1}$ $h^{-1}$).[189] Ji et al. produced 3DOM cubic $SrFeO_{3-\delta}$ using citrate acid–assisted poly (methyl methacrylate)–templating in the presence of surfactants (ethylene glycol, sucrose, or l–lysine). They observed variations in the catalytic activity of the samples, which were correlated with surface area, oxygen adsorption concentration, and low–temperature reduction. Catalytic activity followed the order of $SrFeO_{3-\delta}$–ethylene glycol > $SrFeO_{3-\delta}$–lysine > $SrFeO_{3-\delta}$–glucose (Figure 8e), which correlates with the porosity of the $SrFeO_{3-\delta}$ catalyst.[190] 3DOM $CeMnO_3$ (Figure 8f), 3DOM $LaCoO_3$,[191] and $SmMnO_3$ sheets (Figure 8g) with mesoporous structures display excellent catalytic activity and stability in BTX oxidation.

### 5.3. Effect of Surface Modification

Surface modification of $ABO_3$–PCs using acids, bases, and salts is also an effective approach to enhance catalytic activity.[204–206] Treatment with acids, bases, and salts can increase the specific surface area of the catalyst, etching pores to enhance porosity, and removing the A–site ions to expose active sites.[207]

Acetic acid, citric acid, and nitric acid are commonly employed to improve the performance of $ABO_3$–PCs. Wu et al. investigated the impact of acid treatment on $SmMnO_3$/cordierite monolithic catalysts (**Figure 9a,b**). A series of experiments showed that the catalyst treated with 1.0 mol $L^{-1}$ $HNO_3$ for 6 h and calcined at 450 °C for 1 h has the best performance (Figure 9c), which was attributed to the increase of the specific surface area,

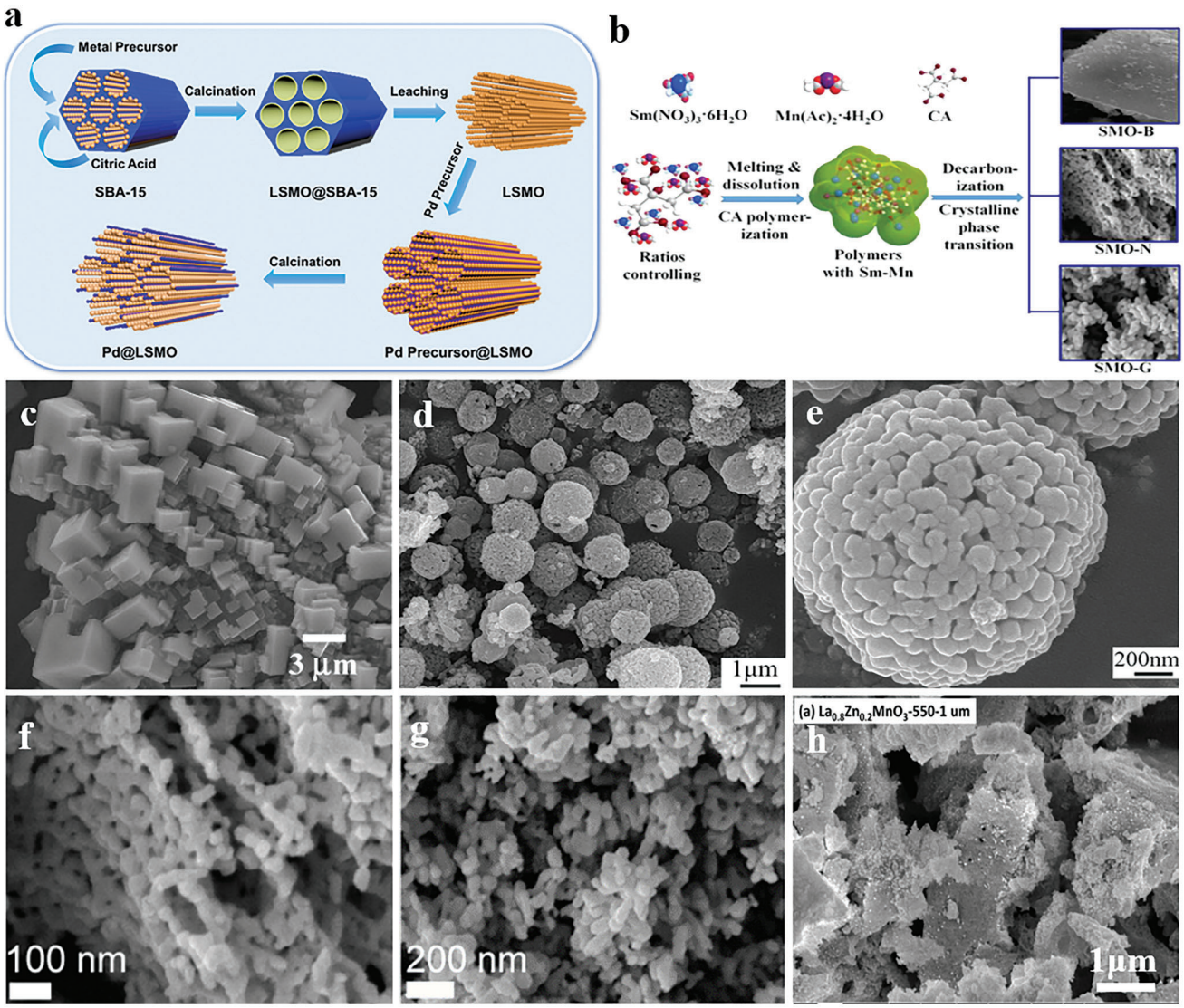


**Figure 7.** a) Route used to prepare Pd/$La_{0.8}Sr_{0.2}MnO_3$ mesoporous nanotube arrays. Reproduced with permission.[148] Copyright 2021, Elsevier. b) Synthesis pathway and SEM images of $SmMnO_3$ with netlike (SMO–N), granular–like (SMO–G), and bulk (SMO–B) structures.[186] Copyright 2018, American Chemical Society. c) SEM image of $La_{0.5}Sr_{0.5}MnO_{3-\delta}$–250. Reproduced with permission.[128] Copyright 2008, Elsevier. d,e) SEM images of the porous spherical $LaMnO_3$ obtained after calcination at 550 °C for 4 h. Reproduced with permission.[187] Copyright 2014, The Royal Society of Chemistry. f) SEM and g) TEM image of $SmMnO_3$ with bulk structures.[186] h) Field emission scanning electron microscopy (FESEM) image of $La_{0.8}Zn_{0.2}MnO_3$–550. Reproduced with permission.[100] Copyright 2021, Elsevier.

pore volume and the mechanical stability of the catalyst.[171] Yang et al. treated $LaCoO_3$ with acetic acid and observed a 40 °C reduction in the temperature required for 90% toluene conversion (Figure 9d–f).[71] Peng et al. modified Sr–doped $LaCoO_3$ using dilute nitric acid and found that the acid treatment improved the stability of the catalyst. Similarly, Li et al. achieved high catalytic activity and stability for toluene oxidation by treating bulk $LaMnO_3$ perovskite with an acidic $KMnO_4$ solution (Figure 9g,h).[156] In the report of Sun et al., citric acid treatment of $GdMnO_3$ resulted in a higher specific surface area, a rich pore structure, abundant high–valent metal ions (Figure 9i) and active oxygen species, consequently improving low–temperature catalytic performance.[85]

Hydrothermal treatment under alkaline conditions may also be used to increase the specific surface area and enrich the oxygen species of the catalyst. As a post–treatment method, Wang et al. obtained rod–like $MnO_2/LaMnO_3$ composite catalysts by combining both alkaline hydrothermal and acid–etching techniques, achieving a $T_{90\%}$ of 236 °C. The $MnO_2/LaMnO_3$ catalyst surface exhibited an elevated $Mn^{4+}/Mn^{3+}$ ratio in comparison to the bulk $LaMnO_3$ catalyst. It significantly improved the low–temperature catalytic activity, thus exhibiting a low apparent activation energy of 38.6 KJ $mol^{-1}$. Additionally, alkali–acid treatment increased the concentration of lattice oxygen on the catalyst surface and generated a high oxygen vacancy density, which facilitates the adsorption of toluene and its subsequent oxidation.

**Table 4.** Shape controlled and structurally optimized $ABO_3$–PCs employed in the catalytic oxidation of benzene and toluene.

| Catalyst | Reactant composition | Space velocity [mL $g^{-1}$ $h^{-1}$] | $T_{50\%}$ [°C] | $T_{90\%}$ [°C] | References |
|---|---|---|---|---|---|
| 3DOM $EuFeO_3$ | 1000 ppm $C_7H_8$ | 20000 | 276 | 322 | [125] |
| 3DOM $Eu_{0.6}Sr_{0.4}FeO_3$ | 1000 ppm $C_7H_8$ | 20000 | 278 | 305 | [125] |
| 3D–$La_{0.6}Sr_{0.4}FeO_{3-\delta}$ | 1000 ppm $C_7H_8$ | 20000 | 225 | 280 | [127] |
| $Ni/La_{0.7}Sr_{0.3}AlO_{3-\delta}$ | 1.5% $C_7H_8$ | 6000 | – | 300 | [134] |
| 3DOM $Co_3O_4/Eu_{0.6}Sr_{0.4}FeO_3$ | 1000 ppm $C_7H_8$ | 20000 | 251 | 269 | [109] |
| Au/3DOM $La_{0.6}Sr_{0.4}MnO_3$ | 1000 ppm $C_7H_8$ | 10000 | 150 | 170 | [147] |
| Hollow spherical $LaCoO_3$ | 1000 ppm $C_7H_8$ | 20000 | 220 | 237 | [155] |
| Rod–like $MnO_2$/$LaMnO_3$ | 1000 ppm $C_7H_8$ | 60000 | – | 236 | [156] |
| 3D–$MnO_2$/$LaMnO_3$ | 2000 ppm $C_7H_8$ | 120000 | 263 | 279 | [158] |
| $SmMnO_3$–B | 1000 ppm $C_6H_6$ | 32000 | 190 | 215 | [186] |
| $SmMnO_3$–N | 1000 ppm $C_6H_6$ | 32000 | 206 | 228 | [186] |
| $SmMnO_3$–G | 1000 ppm $C_6H_6$ | 32000 | 223 | 258 | [186] |
| 3DOM–$SrFeO_{3-\delta}$ | 1000 ppm $C_7H_8$ | 20000 | 292 | 340 | [190] |
| 3D–$LaCoO_3$ | 100 ppm $C_6H_6$ | 40000 | – | 305 | [193] |
| 3D–$La_{0.8}Ce_{0.2}MnO_3$/cordierite | 500 ppm $C_7H_8$ | 6000 | 147 | 217 | [189] |
| Cubic $LaMnO_3$ | 1000 ppm $C_7H_8$ | 20000 | 170 | 220 | [187] |
| Rod–like $MnO_2$/$LaMnO_3$ | 1000 ppm $C_7H_8$ | 60000 | – | 236 | [156] |
| $GdAlO_3$ | 1–2% $C_6H_6$ | – | 259 | – | [194] |
| 3DOM $La_{0.7}Ce_{0.3}CoO_3/Ce_{0.75}Zr_{0.25}O_2$–$Al_2O_3$/cordierite | 1000 ppm $C_7H_8$ | 6000 | 103 | 218 | [195] |
| 3D–$LaMnO_3$ | 1000 ppm $C_7H_8$ | 20000 | 222–232 | 243–253 | [196] |
| 3D–$LaMnO_3$ | 1000 ppm $C_7H_8$ | 20000 | 226 | 249 | [197] |
| Hollow spherical $LaCoO_3$ | 1000 ppm $C_7H_8$ | 20000 | 220 | 237 | [155] |
| 3D–$EuFeO_3$ | 1000 ppm $C_7H_8$ | 20000 | 312 | 347 | [198] |
| 3DOM $CeMnO_3$ | 300 ppm $C_7H_8$ | 15000 | – | 172 | [192] |
| 3D–$Eu_{0.6}Sr_{0.4}FeO_3$ | 1000 ppm $C_7H_8$ | 20000 | 250 | 270 | [199] |
| Spherical $PrMnO_3$ | 1000 ppm $C_7H_8$ | 60000 | >230 | <250 | [200] |
| Cobalt–Enriched $LaCoO_3$ | 1000 ppm $C_7H_8$ | 15000 | 184 | 206 | [201] |
| $La_{0.6}Sr_{0.4}MnO_{3-\delta}$ Microcubes | 1000 ppm $C_7H_8$ | 20000 | 283 | – | [202] |
| 3DOM– $La_{0.7}Ce_{0.3}CoO_3$ | 1000 ppm $C_7H_8$ | 6000 | 103 | 218 | [203] |

### 5.4. Effect of Humidity

Water vapor is one of the products of BTX oxidation and is also commonly present in exhaust gases,[208,209] and has two key effects on the catalyst.[210] Water can adsorb onto active sites of the catalyst, competing with BTX for adsorption and inhibiting the oxidation process, and can also act as an efficient cleaning agent, removing byproducts from the surface of the catalysts.[211,212]

Zhao et al. confirmed that humidity has an inhibitory effect on toluene oxidation,[126] consuming the active oxygen atoms adsorbed by the catalyst and blocking the active sites through the generation of surface bound OH species (**Figure 10a**). In another study, water vapor was introduced into the reaction using 6.4Au/LSMO PC a 2% decrease in the $T_{90\%}$ for toluene oxidation was observed.[147] However, deactivation of the 6.4Au/LSMO catalyst is reversible, with activity restored when the water is removed from the system (Figure 10b). Additionally, the impact of water on LSMO was investigated, revealing a decrease in conversion of toluene to 95 and 86% when 5 and 10 vol.% of water were introduced, respectively.[97] Upon the removal of water, toluene conversion returned to the initial level (Figure 10c). Similar to the above results, in other study water was shown to reduce the activity of $1.67Mn_3O_4$–2Au/3DOM $La_{0.6}Sr_{0.4}CoO_3$, 5.92Au/8$MnO_x$/3DOM $La_{0.6}Sr_{0.4}CoO_3$ (x = 2–4), $SmMnO_3$ cordierite monolithic and $LaCoO_3$ PCs (Figure 10d,e).

In addition to inhibiting the activity of $ABO_3$-PCs, the introduction of water vapor may also affect the $CO_2$ yield. For instance, Sun et al. found that different humidity conditions (0, 50, and 100% relative humidity) did not affect the conversion of toluene but led to a decrease in the yield of $CO_2$ at 230 °C (Figure 10f),[186] with the oxidation of carboxyl group-containing and carbonate intermediates being incomplete. Water vapor may also promote the conversion of CO to $CO_2$ through the water-gas shift reaction (WGSR) to improve the $CO_2$ yield.[213,214]

### 5.5. Effect of Sulfur Species

It is widely recognized that many industrial emissions often contain a diverse range of sulfur species,[215] with many sulfur species acting as catalyst poisons.[216–218] Various sulfur species ($SO_2$, $SO_3$, $SO_3^{2-}$, $SO_4^{2-}$, and $S^{2-}$) can deposit on a catalyst surface to block active sites,[219] preventing the adsorption and diffusion of BTX and catalyst deactivation.[220,221] Not surprisingly,

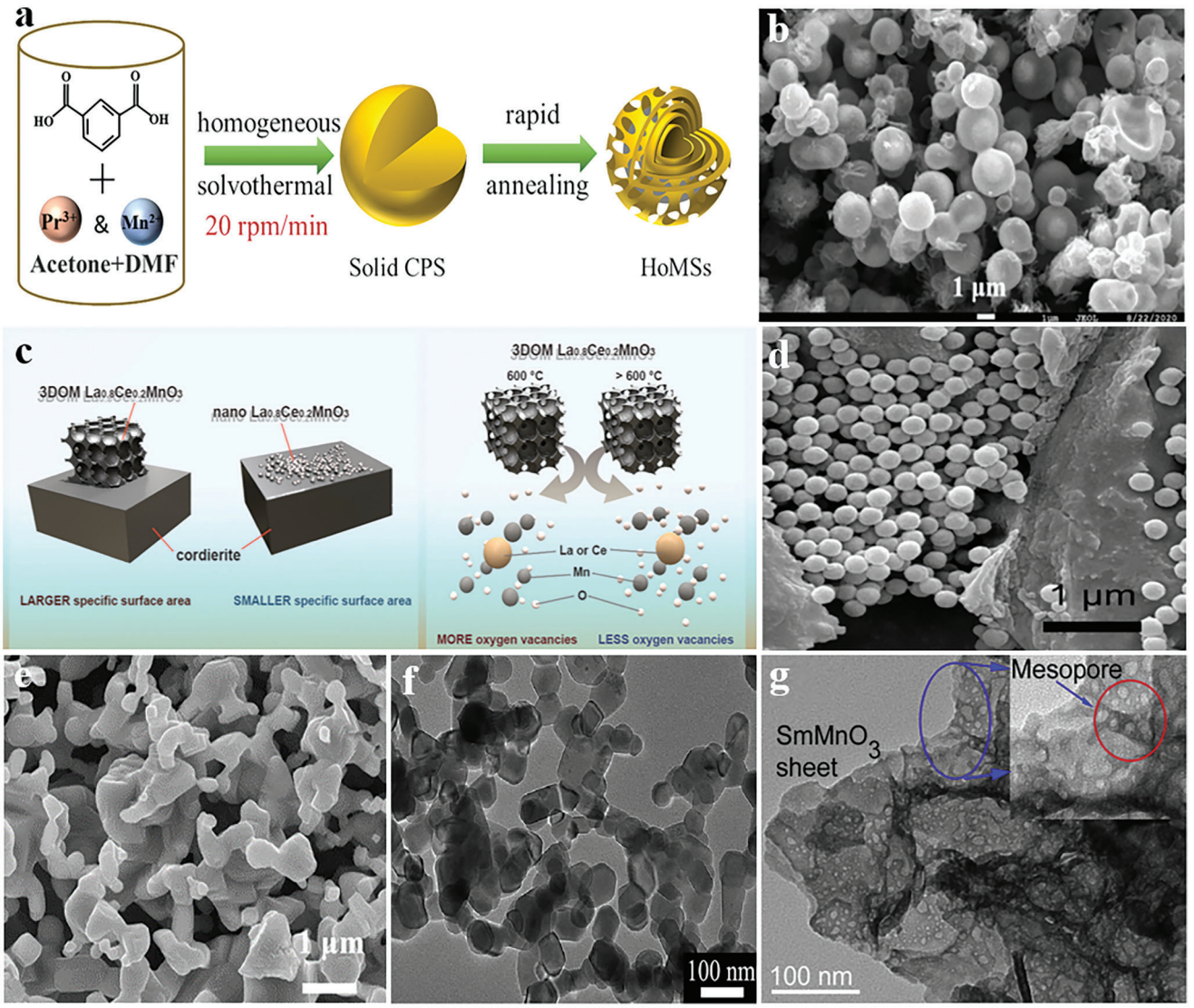


**Figure 8.** a) Hollow multishell spherical $PrMnO_3$–HoMS PC that efficiently catalyzes oxidation of toluene. b) FESEM image of the $PrMnO_3$–HoMSs. Reproduced with permission.[188] Copyright 2021, Elsevier. c) Comparison of 3DOM $La_{0.8}Ce_{0.2}MnO_3$/cordierite and nano $La_{0.8}Ce_{0.2}MnO_3$/cordierite catalysts. d) SEM image of 3DOM–LCM/cordierite. Reproduced with permission.[189] Copyright 2019, Elsevier. e) SEM image of $SrFeO_{3-\delta}$–bulk–900 PCs.[190] f) HRTEM of 3DOM $CeMnO_3$. Reproduced with permission.[190] Copyright 2021, Elsevier. Reproduced with permission.[192] Copyright 2020, Elsevier. g) Mesoporous structured $SmMnO_3$ sheets. Reproduced with permission.[82] Copyright 2018, Elsevier.

extensive research has been conducted to investigate the impact of $SO_2$ on the activity of $ABO_3$–PCs.

Hu et al. used a sol–gel method to prepare $La_{1-x}Ce_xCo_{1-y}Fe_yO_3$ (x = 0, 0.2, 0.4, and 0.6; y = 0, 0.2, 0.4, and 0.6) catalysts, with $Ce^{4+}$ or $Fe^{3+}$ doped $LaCoO_3$ showing improved the catalytic activity in the oxidation of toluene and resistance to sulfur poisoning (**Figure 11a**).[107] Analysis of sulfate species in sulfur-aged catalysts during the temperature-programming stages revealed $Ce^{4+}$ substitution improved catalytic activity, whereas $Fe^{3+}$ substitution enhanced resistance to poisoning by sulfur (Figure 11b). During the oxidation of toluene, sulfate concentrations were observed to decrease with increasing temperatures, suggesting that heating caused sulfate poisoning and the adsorption of gaseous $SO_2$ on surface anion vacancies, forming sulfite or sulfate via continuous oxidation.[222] The process of catalyst poisoning by $SO_2$ was evident via the formation of lanthanum sulfate and sulfite species, i.e. extracting an active component from the PC. However, by substituting B–site cations (i.e. $LaCo_{1-x}M_xO_3$), Chen et al. showed that the negative effects of $SO_2$ poisoning could be reduced.[79] Metal ions influence factors such as lattice stability and sulfur adsorption (Figure 11c). $Fe^{3+}$ doping was found to afford a more effective catalyst compared to catalysts doped with $Cr^{3+}$ or $Cu^{2+}$, improving the tolerance to sulfur compounds (Figure 11d).

Huang et al. examined the influence of $SO_2$ and dodecyl mercaptan on $La_{0.8}Sr_{0.2}MnO_3$ and $La_{0.8}Cu_{0.2}MnO_3$ PCs during the oxidation of toluene.[110] They observed that the PCs were poisoned in the presence of $SO_2$. In the presence of dodecyl mercaptan

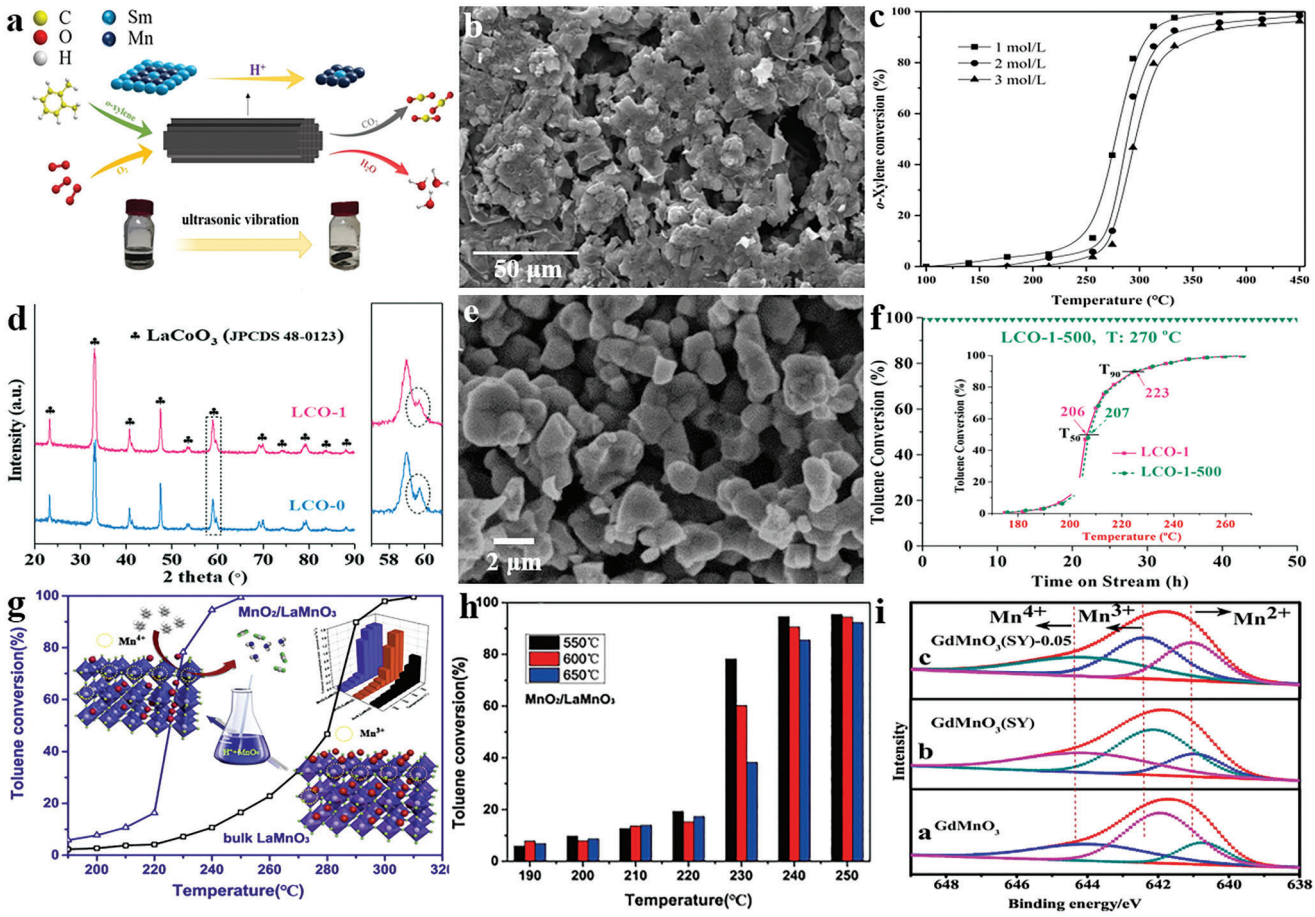


**Figure 9.** a) Preparation and application of the $SmMnO_3$/cordirite monolithic catalyst. b) SEM image of the $SmMnO_3$/cordierite catalyst treated with 1 mol $L^{-1}$ $HNO_3$ for 6 h. c) Catalytic activity of the $SmMnO_3$/cordierite acid–treated with different concentrations of $HNO_3$. Reproduced with permission.[171] Copyright 2021, Chemistry Europe. d) XRD patterns of raw $LaCoO_3$ catalyst (LCO–0) and the $LaCoO_3$ treated with acetic acid for 1 h (LCO–1). e) SEM image of LCO–1. f) Toluene conversions of LCO–1–500 at 270 °C. Reproduced with permission.[71] Copyright 2018, John Wiley and Sons. g) Catalytic activity of $MnO_2/LaMnO_3$ and bulk $LaMnO_3$ catalysts in the oxidation of toluene. h) Toluene conversions catalyzed by $MnO_2/LaMnO_3$.[156] i) XPS spectra of Mn2p3/2: a–$GdMnO_3$, b–$GdMnO_3$ (SY), and c–$GdMnO_3$ (SY)-0.05. Reproduced with permission.[156] Copyright 2019, Elsevier.

($C_{12}H_{25}SH$), $La_{0.8}Sr_{0.2}MnO_3$ exhibits better resistance to sulfur poisoning than $La_{0.8}Cu_{0.2}MnO_3$. It was found that the $SO_2$ deactivation is due to the formation of $CuSO_4$ on the catalyst surface (Figure 11e,f).

## 6. Mechanistic Insights

There is a lack of consensus on the reaction mechanism of catalytic oxidation by $ABO_3$-PCs catalysts. Proposed kinetics encompass Langmuir Hinshelwood (L–H), Eley Rideal (E–R), and Mars van Krevelen (MvK) mechanisms. The L–H mechanism implies that the catalytic reaction occurs between adsorbed oxygen and adsorbed BTX. The E–R mechanism implies that the reaction takes place between adsorbed oxygen and gaseous substrates. The MvK mechanism is widely used to rationalize the low–temperature-catalytic oxidation of BTX, and involves a dynamic cycle where the catalyst undergoes simultaneous reduction and oxidation. This mechanism relies on chemisorbed oxygen and lattice oxygen in the catalyst, in contrast to the L–H and E–R mechanisms that rely on adsorbed oxygen species on the catalyst surface.

In the vast majority of current studies, the oxidation of BTXs over $ABO_3$-PCs catalysts mainly follows the redox mechanism (MvK) and is divided into two main steps:

1) BTXs diffuse and adsorbed on the catalyst surface where they are oxidized to $CO_2$ and $H_2O$ by reaction with the lattice oxygens on the catalyst surface, and at the same time, the catalyst surface is reduced due to the generation of oxygen vacancies.
2) The oxygen adsorbed by the catalyst dissociates and fill the oxygen vacancies to re-oxidize the surface atoms.

This mechanism achieves the oxidation of BTXs by changes of the metal valence states, $O_{latt}$ and $O_{ads}$, in the catalyst. As shown in **Figure 12**, usually a series of intermediates are formed followed by further chemical bond breaking and reorganization, resulting in the full conversion of BTXs to $CO_2$ and $H_2O$. This mechanism has been confirmed by many studies. For example, Xiang et al. explored the mechanism of toluene oxidation by

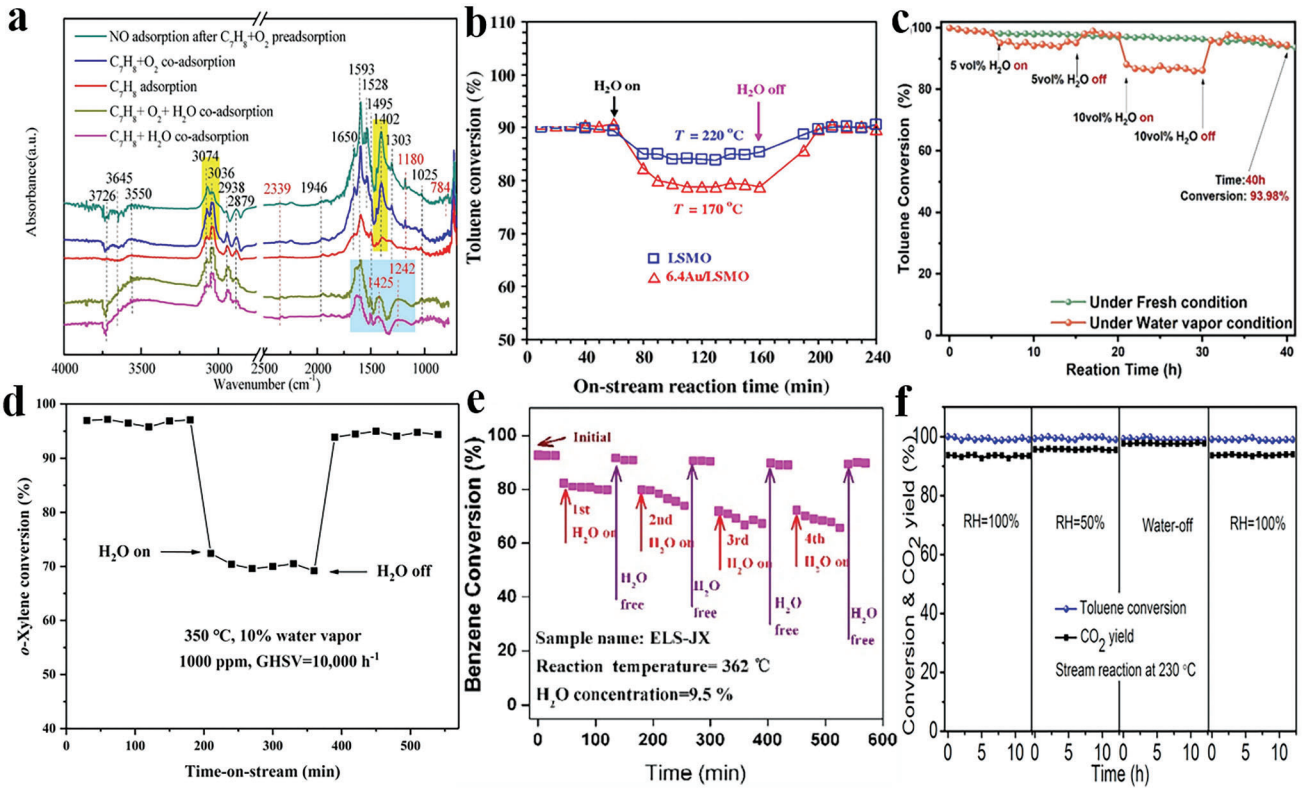


**Figure 10.** a) In situ DRIFTS of $La_{0.65}Co_{0.35}FeO_3$ in the presence of toluene, toluene and $O_2$, toluene and $H_2O$, and toluene and $O_2$ and $H_2O$.[126] Impact of $H_2O$ on toluene oxidation using b) the Au/3DOM $La_{0.6}Sr_{0.4}MnO_3$ catalyst and c) the La–Sr–Co–Fe–O perovskite–type oxides. Reproduced with permission.[97] Copyright 2023, Elsevier. d) Impact of $H_2O$ on *o*–xylene oxidation using the $SmMnO_3$ cordierite monolithic catalyst. Reproduced with permission.[171] Copyright 2021, John Wiley and Sons. e) Impact of $H_2O$ on benzene oxidation using the $LaCoO_3$/SBA–15. Reproduced with permission.[65] Copyright 2017, Elsevier. f) Impact of $H_2O$ on toluene oxidation using the $SmMnO_3$ with a netlike structure. Reproduced with permission.[186] Copyright 2018, American Chemical Society.

$LaFeO_3$ and showed that toluene is adsorbed on the surface of the $LaFeO_3$ catalyst, with the chemisorbed species then reacting with ambient oxygen atoms to form carbonates, which are then converted to $CO_2$ and desorbed.[72] During the oxidation of BTX, a series of intermediates such as benzoic acid, maleic anhydride and carboxybenzene species are generated.[116] A variety of intermediates were identified from the oxidation of BTX catalyzed by $\gamma$-$MnO_2$/$SmMnO_3$, including 5-hexen-1-ol, ethanedioicacid, acetic acid, n-butyric acid, phenol, and malic acid for benzene oxidation; acetic acid, benzaldehyde, 2-(5H)-furanone, citric acid and benzoic acid for toluene oxidation and acetic acid, citric acid, and 1,3-isobenzofurandione for *o*-xylene.

During the reaction, ABO3-PC catalysts may degradate and deactivate, primarily through mechanisms such as poisoning, coking, plugging, and sintering.[45] Catalyst poisons such as sulfides or chlorides can form strong chemical bonds with the active components of $ABO_3$-PC, thereby reducing or eliminating its activity.[229] Simultaneously, during the catalytic process, the deposition of carbon-containing substances or other intermediates in the pores of the catalyst can coat the active catalytic sites and block micropores, hindering the diffusion of BTX molecules into the pores, resulting in catalyst inactivation.[230] Moreover, high temperatures can induce structural and performance changes in the catalyst. Elevated temperatures can lead to sintering, reducing catalytic efficiency, as well as altering the chemical and phase composition of the catalyst.[231] These changes may include grain growth, burial of active components by the carrier, and loss of active components due to the generation of volatile or sublimable substances.[232] Further research is required to understand the intricate decomposition and deactivation processes, as well as the catalytic mechanisms during reactions more thoroughly.

## 7. Conclusion and Outlook

Catalytic oxidation is an important process for the elimination of organic pollutants such as BTX, especially when the concentration of these pollutants is low. Generally, the most active catalysts are based on precious and expensive noble metal oxides. However, in recent years, $ABO_3$–PCs have been widely studied as BTX oxidation catalysts, and are particularly versatile due to their flexible composition, abundant defects, highly exposed active surfaces, and tunable redox properties. Moreover, $ABO_3$–PCs display high activity and stability in the catalytic oxidation of BTX.

The main role of the A-site ions ($La^{3+}$, $Ce^{4+}$, $Sr^{2+}$, $Ca^{2+}$, etc.) of $ABO_3$-PCs is to stabilize the chalcogenide crystal structure. However, the A-site ions can introduce lattice defects and change the chemical sites of the lattice oxygens, affecting the dispersion and valence of the B-site ions, thus indirectly altering the activity

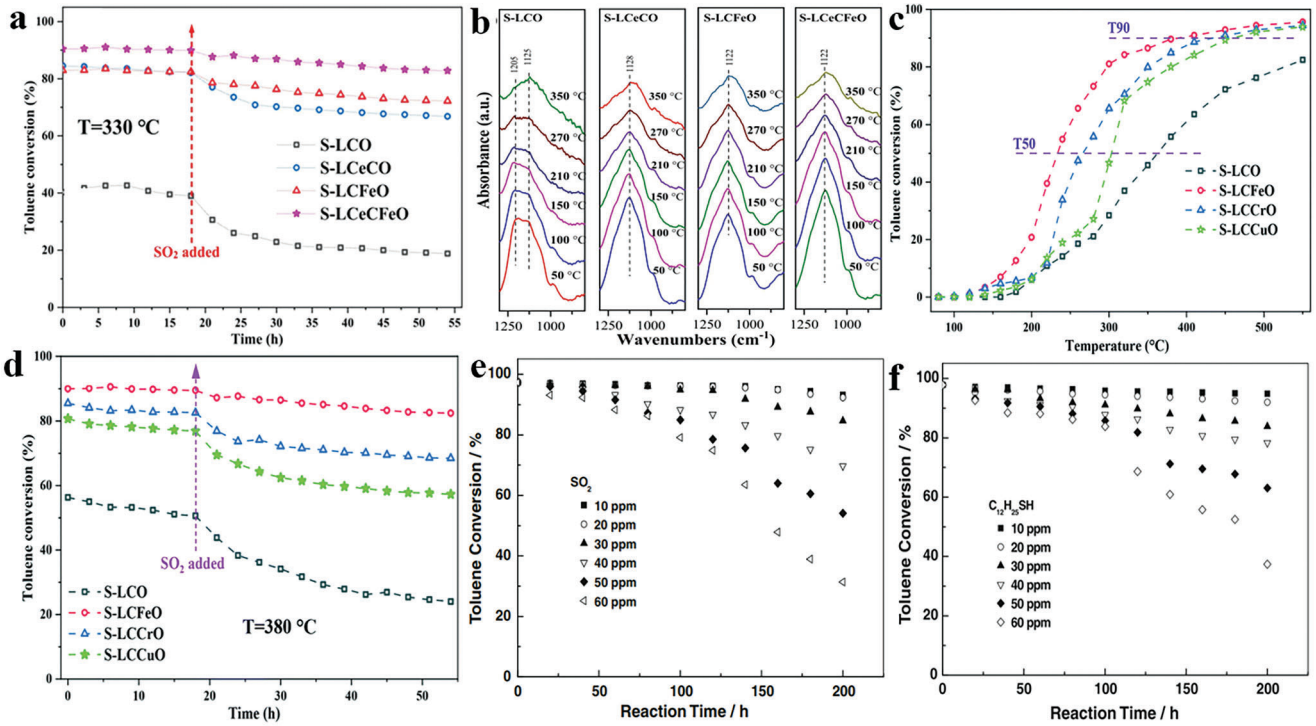


**Figure 11.** a) Impact of $SO_2$ on toluene oxidation of sulfur–aged catalysts.[107] b) Infrared spectra of sulfate in the heating process of toluene oxidation for S–LCO, S–LCeCO, S–LCFeO, and S–LCeCFeO catalysts. c) Conversion of toluene as a function of temperature catalyzed by S-LCO, S–LCFeO, S–LCCrO, and S–LCCuO. d) Catalytic stability test for toluene oxidation of sulfur–aged catalysts list in (c). e) Impact of $SO_2$ on the conversion of toluene catalyzed by $La_{0.8}Sr_{0.2}MnO_3$ over time. f) Impact of $C_{12}H_{25}SH$ on the conversion of toluene by $La_{0.8}Cu_{0.2}MnO_3$. Reproduced with permission.[110] Copyright 2010, Elsevier.

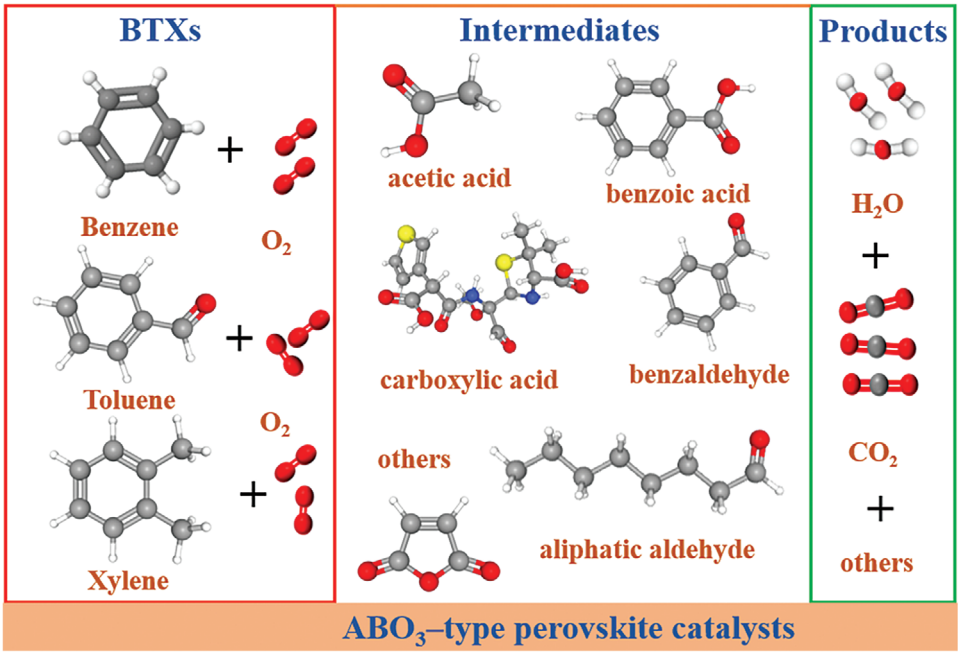


**Figure 12.** Intermediates observed in the catalytic oxidation of BTX by $ABO_3$–PCs.

of $ABO_3$-PCs. Usually, the catalytic activity of $ABO_3$-PCs is determined by the B-site ions ($Co^{2+}$, $Fe^{3+}$, $Mn^{3+}$, $Ni^{3+}$, $Cu^{2+}$, etc.), which exhibit a variety of oxidation states and have high structural/compositional flexibility and redox capacities.

$ABO_3$-PCs are often used as supports to immobilize noble metal particles or are themselves immobilized on metal oxides and other materials, increasing the specific surface area of the active catalyst, leading to improved activity. In addition, different morphologies and structures of $ABO_3$-PCs affect the packing density, porosity, specific surface area, and surface energy of the catalyst, influencing catalytic activity.

The catalytic activity is also affected by water, sulfur species, and other impurities. Water can adsorb onto the active sites of the catalyst, competing with BTX for adsorption and inhibiting the oxidation process. Sulfur species tend to deposit on the surface of $ABO_3$–PCs, blocking the active sites, hindering the adsorption and diffusion of BTX, and extruding metal ions that react to form catalytically inactive sulfates.

The mechanism of benzene and toluene oxidation by $ABO_3$–PCs mainly follows the MvK mechanism, whereas the oxidation mechanism of xylene and BTX mixtures, has not been fully explored and there are a lack of mechanistic studies exploring real flue gases contain BTX. In addition to A-site, B-site doping, and A/B-site co-doping, anion doping on the O-site has recently emerged as an alternative approach to tune the electronic structure of $ABO_3$–PCs to improve catalytic performance, and further studies are required in this nascent area.[144] In situ spectroscopic and theoretical studies are required to further clarify BTX oxidations using $ABO_3$–PCs, and upscaling is also essential, to better understand potential problems such as coking, poisoning, and sintering. Employing in–situ characterization techniques, like in situ Raman spectroscopy.

Although challenges persist, $ABO_3$–PC are promising candidates for application as real-world BTX oxidations. As $ABO_3$–PCs continue to improve, they are likely to contribute to pollution control and the preservation of health and the environment. Combining $ABO_3$ perovskite oxidation processes with lead halide perovskite photovoltaics[223–226] would also provide a sustainable way to achieve BTX oxidation and capturing the $CO_2$ generated would allow clean synthetic fuels to be obtained.[227,228]

## Acknowledgements

J.Y. and G.L. contributed equally to this work. The authors thank the Shanghai "Science and Technology Innovation Action Plan" – Baoshan Transformation Development Science and Technology Special Project (21SQBS01100), the National Natural Science Foundation of China (22276137 and 52170087), the Fundamental Research Funds for the Central Universities and the EPFL for financial support. The authors thank the Fonds national Suisse de la recherche scientifique (FNS) – MINT under contract number 200020E_211193 and the German Science Foundation (DFG) program SPP2196 under project No: 424101351.

Open access funding provided by Ecole Polytechnique Federale de Lausanne.

## Conflict of Interest

The authors declare no conflict of interest.

## Keywords

BTX, catalytic oxidation, environmental sustainability, perovskites

Received: January 22, 2024
Revised: March 21, 2024
Published online:

[1] S. Li, Y. Lin, G. Liu, C. Shi, *Environ. Sci.: Processes Impacts* **2023**, *25*, 727.
[2] K. Hui, Y. Yuan, B. Xi, W. Tan, *Environ. Int.* **2023**, *172*, 107799.
[3] Y.-S. Son, *Chem. Eng. J.* **2017**, *316*, 609.
[4] Y. Liu, M. Shao, L. Fu, S. Lu, L. Zeng, D. Tang, *Atmos. Environ.* **2008**, *42*, 6247.
[5] F. Simantiraki, E. Gidarakos, *J. Environ. Manage* **2015**, *159*, 218.
[6] W.-C. Cho, K.-M. Poo, H. O. Mohamed, T.-N. Kim, Y.-S. Kim, M. H. Hwang, D.-W. Jung, K.-J. Chae, *Chemosphere* **2018**, *206*, 483.
[7] G. Gan, S. Fan, X. Li, Z. Zhang, Z. Hao, *J. Environ. Sci.* **2023**, *123*, 96.
[8] X. Zhang, B. Gao, A. E. Creamer, C. Cao, Y. Li, *J. Hazard. Mater.* **2017**, *338*, 102.
[9] K. Vellingiri, V. Choudhary, S. Kumar, L. Philip, *Environ. Sci.: Water Res. Technol.* **2022**, *8*, 1359.
[10] W. Tang, G. Liu, D. Li, H. Liu, X. Wu, N. Han, Y. Chen, *Sci. China: Chem.* **2015**, *58*, 1359.
[11] Z. Zhang, Z. Jiang, W. Shangguan, *Catal. Today* **2016**, *264*, 270.
[12] M. S. Kamal, S. A. Razzak, M. M. Hossain, *Atmos. Environ.* **2016**, *140*, 117.
[13] S. Scirè, L. F. Liotta, *Appl. Catal., B* **2012**, *125*, 222.
[14] R. Zhao, H. Wang, D. Zhao, R. Liu, S. Liu, J. Fu, Y. Zhang, H. Ding, *Int. J. Mol. Sci.* **2022**, *23*, 13739.
[15] C. Liang, C. Li, Y. Zhu, X. Du, C. Yao, Y. Ma, J. Zhao, *Chem. Eng. J.* **2023**, *455*, 140461.
[16] Z. Zhicheng, J. Tingting, L. Tao, Z. Shourong, *New J. Chem.* **2023**, *47*, 10289.
[17] C. Cheng, L. Chang, X. Zhang, Q. Deng, H. Chai, Y. Huang, *Environ. Res.* **2023**, *229*, 115994.
[18] J. He, X. Xu, M. Li, S. Zhou, W. Zhou, *Anal. Chim. Acta* **2023**, *1251*, 341007.
[19] X. Xu, W. Wang, W. Zhou, Z. Shao, *Small Methods* **2018**, *2*, 1800071.
[20] A. L. Kustov, O. P. Tkachenko, L. M. Kustov, B. V. Romanovsky, *Environ. Int.* **2011**, *37*, 1053.
[21] N. Rezlescu, E. Rezlescu, P. Dorin Popa, C. Doroftei, M. Ignat, *Ceram. Int.* **2015**, *41*, 4430.
[22] K. Everaert, J. Baeyens, *J. Hazard. Mater.* **2004**, *109*, 113.
[23] S. M. D. A. G. U. Souza, A. D. da Luz, A. da Silva, A. A. U. de Souza, *Ind. Eng. Chem. Res.* **2012**, *51*, 6461.
[24] C. He, J. Cheng, X. Zhang, M. Douthwaite, S. Pattisson, Z. Hao, *Chem. Rev.* **2019**, *119*, 4471.
[25] C. Li, Y. Zhao, H. Song, H. Li, *J. Chem. Technol. Biotechnol.* **2020**, *95*, 2069.
[26] D. Paneva, M. Dimitrov, N. Velinov, H. Kolev, V. Kozhukharov, T. Tsoncheva, I. Mitov, *J. Phys.: Conf. Ser.* **2010**, *217*, 012043.
[27] C. Liu, Y. Xin, C. Zhang, J. Liu, P. Liu, X. He, Y. Mu, *Sci. Total Environ.* **2023**, *855*, 158873.
[28] G. I. Asejeje, A. R. Ipeaiyeda, P. C. Onianwa, *Environ. Sci. Pollut. Res. Int.* **2021**, *28*, 15361.
[29] Y. Dumanoglu, M. Kara, H. Altiok, M. Odabasi, T. Elbir, A. Bayram, *Atmos. Environ.* **2014**, *98*, 168.
[30] E. Lopez, M. Schuhmacher, J. L. Domingo, *Environ. Sci. Pollut. Res. Int.* **2008**, *15*, 278.
[31] H. Rajabi, M. Hadi Mosleh, P. Mandal, A. Lea-Langton, M. Sedighi, *Sci. Total Environ.* **2020**, *727*, 138654.

[32] C. Zhang, C. Wang, S. Gil, A. Boreave, L. Retailleau, Y. Guo, J. L. Valverde, A. Giroir-Fendler, *Appl. Catal., B* **2017**, *201*, 552.
[33] H. Einaga, S. Hyodo, Y. Teraoka, *Top. Catal.* **2010**, *53*, 629.
[34] T. Sukaram, T. Apiparakoon, T. Tiyarattanachai, D. Ariyaskul, K. Kulkraisri, S. Marukatat, R. Rerknimitr, R. Chaiteerakij, *Diagnostics (Basel)*. **2023**, *13*, 257.
[35] D.-L. Yang, Z.-N. Zhang, H. Liu, Z.-Y. Yang, M.-M. Liu, Q.-X. Zheng, W. Chen, P. Xiang, *Chemosphere* **2022**, *311*, 137037.
[36] Y. Wang, X. Han, J. Li, L. Zhang, Y. Liu, R. Jin, L. Chen, X. Chu, *Chemosphere* **2023**, *327*, 138425.
[37] Y. Zhang, Y. Wang, R. Xie, H. Huang, M. K. H. Leung, J. Li, D. Y. C. Leung, *Environ. Sci. Technol.* **2022**, *56*, 16582.
[38] K. Zhang, H. Ding, W. Pan, X. Mu, K. Qiu, J. Ma, Y. Zhao, J. Song, Z. Zhang, *Environ. Sci. Technol.* **2022**, *56*, 9220.
[39] J. Zhang, X. Xu, S. Zhao, X. Meng, F.-S. Xiao, *Catal. Today* **2023**, *410*, 56.
[40] M. Zang, C. Zhao, Y. Wang, S. Chen, *J. Saudi Chem. Soc.* **2019**, *23*, 645.
[41] Q. Yu, C. Li, D. Ma, J. Zhao, X. Liu, C. Liang, Y. Zhu, Z. Zhang, K. Yang, *Coord. Chem. Rev.* **2022**, *471*, 214738.
[42] M. Ao, G. H. Pham, V. Sage, V. Pareek, *J. Mol. Catal. A: Chem.* **2016**, *416*, 96.
[43] Y. Yang, S. Zhao, L. Cui, F. Bi, Y. Zhang, N. Liu, Y. Wang, F. Liu, C. He, X. Zhang, *Green Energy Environ.* **2022**.
[44] L. Yang, Y. Li, Y. Sun, W. Wang, Z. Shao, *Energy. Environ. Mater.* **2022**, *5*, 751.
[45] C. Yang, G. Miao, Y. Pi, Q. Xia, J. Wu, Z. Li, J. Xiao, *Chem. Eng. J.* **2019**, *370*, 1128.
[46] P. Wu, X. Jin, Y. Qiu, D. Ye, *Environ. Sci. Technol.* **2021**, *55*, 4268.
[47] P. Wang, X. Ma, X. Hao, B. Tang, A. Abudula, G. Guan, *Catal. Rev.* **2022**, 2078555.
[48] M. Tomatis, H. H. Xu, J. He, X. Zhang, *J. Chem.* **2016**, *2016*, 8324826.
[49] Y. Su, K. Fu, C. Pang, Y. Zheng, C. Song, N. Ji, D. Ma, X. Lu, C. Liu, R. Han, Q. Liu, *Environ. Sci. Technol.* **2022**, *56*, 9854.
[50] M. A. Salaev, A. A. Salaeva, T. S. Kharlamova, G. V. Mamontov, *Appl. Catal., B* **2021**, *295*, 120286.
[51] D. Murindababisha, A. Yusuf, Y. Sun, C. Wang, Y. Ren, J. Lv, H. Xiao, G. Z. Chen, J. He, *Environ. Sci. Pollut. Res. Int.* **2021**, *28*, 62030.
[52] R. Liu, H. Wu, J. Shi, X. Xu, D. Zhao, M. Zhang, S. Liu, H. Ding, *Catal. Sci. Technol.* **2022**, *12*, 6945.
[53] F. Lin, Z. Zhang, N. Li, B. Yan, C. He, Z. Hao, G. Chen, *Chem. Eng. J.* **2021**, *404*, 126534.
[54] J. Niu, W. Liu, H. Dai, H. He, X. Zi, P. Li, *Chin. Sci. Bull.* **2006**, *51*, 1673.
[55] W. B. Li, J. X. Wang, H. Gong, *Catal. Today* **2009**, *148*, 81.
[56] H. Einaga, Y. Nasu, M. Oda, H. Saito, *Chem. Eng. J.* **2016**, *283*, 97.
[57] N. Labhasetwar, G. Saravanan, S. Kumar Megarajan, N. Manwar, R. Khobragade, P. Doggali, F. Grasset, *Sci. Technol. Adv. Mater.* **2015**, *16*, 036002.
[58] I. Alxneit, A. Garbujo, G. Carollo, D. Ferri, A. Glisenti, *Phys. Chem. Chem. Phys.* **2020**, *22*, 18798.
[59] Y. Guo, M. Wen, G. Li, T. An, *Appl. Catal., B* **2021**, *281*, 119447.
[60] K. Fu, Y. Su, Y. Zheng, R. Han, Q. Liu, *Chemosphere* **2022**, *308*, 136256.
[61] R. Spinicci, M. Faticanti, P. Marini, S. De Rossi, P. Porta, *J. Mol. Catal. A: Chem.* **2003**, *197*, 147.
[62] C. Zhang, Y. Guo, Y. Guo, G. Lu, A. Boreave, L. Retailleau, A. Baylet, A. Giroir-Fendler, *Appl. Catal., B* **2014**, *148–149*, 490.
[63] M. Wu, H. Li, S. Ma, S. Chen, W. Xiang, *Sci. Total Environ.* **2021**, *795*, 148904.
[64] N. Rezlescu, E. Rezlescu, P. D. Popa, C. Doroftei, M. Ignat, *Composites, Part B* **2014**, *60*, 515.
[65] Y. Luo, K. Wang, J. Zuo, Q. Qian, Y. Xu, X. Liu, H. Xue, Q. Chen, *Mol. Catal.* **2017**, *436*, 259.
[66] Y. Luo, K. Wang, J. Zuo, Q. Qian, Y. Xu, X. Liu, H. Xue, Q. Chen, *Catal. Sci. Technol.* **2017**, *7*, 496.
[67] M. Keller, H. Leion, T. Mattisson, *Appl. Catal., B* **2016**, *183*, 298.
[68] C. Hu, Q. Zhu, Z. Jiang, *Powder Technol.* **2009**, *194*, 109.
[69] J. Zhang, D. Tan, Q. Meng, X. Weng, Z. Wu, *Appl. Catal., B* **2015**, *172–173*, 18.
[70] R. Z. Yarbay Şahin, M. Duplančić, V. Tomašić, J. H. Badia i Córcoles, S. Kurajica, *Int. J. Environ. Sci. Technol.* **2021**, *19*, 553.
[71] Q. Yang, D. Wang, C. Wang, X. Li, K. Li, Y. Peng, J. Li, *Catal. Sci. Technol.* **2018**, *8*, 3166.
[72] M. Wu, S. Ma, S. Chen, W. Xiang, *J. Cleaner Prod.* **2020**, *277*, 123224.
[73] M. Wu, S. Chen, W. Xiang, *Chem. Eng. J.* **2020**, *387*, 124101.
[74] K. Soongprasit, D. Aht-Ong, V. Sricharoenchaikul, D. Atong, *Top. Catal.* **2013**, *56*, 339.
[75] Z. Sihaib, F. Puleo, G. Pantaleo, V. La Parola, J. L. Valverde, S. Gil, L. F. Liotta, A. Giroir-Fendler, *Catalysts* **2019**, *9*, 226.
[76] Z. Sihaib, F. Puleo, J. M. Garcia-Vargas, L. Retailleau, C. Descorme, L. F. Liotta, J. L. Valverde, S. Gil, A. Giroir-Fendler, *Appl. Catal., B* **2017**, *209*, 689.
[77] G. Pecchi, M. G. Jiliberto, E. J. Delgado, L. E. Cadús, J. L. G. Fierro, *J. Chem. Technol. Biotechnol.* **2011**, *86*, 1067.
[78] A. Musialik-Piotrowska, H. Landmesser, *Catal. Today* **2008**, *137*, 357.
[79] C. Lv, M. Hu, T. Yuan, L. Yan, H. Chen, *Catal. Sci. Technol.* **2022**, *12*, 3670.
[80] Y. Liu, H. Dai, J. Deng, Y. Du, X. Li, Z. Zhao, Y. Wang, B. Gao, H. Yang, G. Guo, *Appl. Catal., B* **2013**, *140–141*, 493.
[81] L. Liu, J. Sun, J. Ding, Y. Zhang, J. Jia, T. Sun, *Inorg. Chem.* **2019**, *58*, 14275.
[82] L. Liu, J. Jia, T. Sun, H. Zhang, *Mater. Lett.* **2018**, *212*, 107.
[83] B. Li, Q. Yang, Y. Peng, J. Chen, L. Deng, D. Wang, X. Hong, J. Li, *Chem. Eng. J.* **2019**, *366*, 92.
[84] S. A. Hosseini, M. T. Sadeghi, *Chin. J. Catal.* **2010**, *31*, 747.
[85] M. Guo, L. Liu, J. Gu, H. Zhang, X. Min, J. Liang, J. Jia, K. Li, T. Sun, *Chin. J. Chem. Eng.* **2021**, *34*, 278.
[86] A. Giroir-Fendler, M. Alves-Fortunato, M. Richard, C. Wang, J. A. Díaz, S. Gil, C. Zhang, F. Can, N. Bion, Y. Guo, *Appl. Catal., B* **2016**, *180*, 29.
[87] B. Gao, J. Deng, Y. Liu, Z. Zhao, X. Li, Y. Wang, H. Dai, *Chin. J. Catal.* **2013**, *34*, 2223.
[88] X. Fei, W. Jia, Z. Hou, H. Dai, Q. Shan, D. Hei, Y. Ling, *Radiat. Phys. Chem.* **2019**, *158*, 143.
[89] H. Bai, Z. Wang, J. Zhang, J. Wu, Y. Yue, Q. Liu, G. Qian, *J. Environ. Manage.* **2021**, *294*, 113025.
[90] W. Wang, M. Xu, X. Xu, W. Zhou, Z. Shao, *Angew. Chem., Int. Ed.* **2019**, *59*, 136.
[91] R. Zhang, D. Shi, N. Liu, Y. Cao, B. Chen, *Appl. Catal., B* **2014**, *146*, 79.
[92] P. K. Yadav, S. Kumari, U. Naveena, P. A. Deshpande, S. Sharma, *Appl. Catal., A* **2022**, *643*, 118768.
[93] G. Liu, J. Li, K. Yang, W. Tang, H. Liu, J. Yang, R. Yue, Y. Chen, *Particuology* **2015**, *19*, 60.
[94] J. Hu, J. Zhou, T. Zhang, S. Liu, K. Du, *Korean J. Chem. Eng.* **2022**, *39*, 3032.
[95] B. Heidinger, S. Royer, J.-M. Giraudon, O. Gardoll, H. Alamdari, J.-F. Lamonier, *ChemCatChem* **2020**, *12*, 2271.
[96] S. Qi, W. Zhang, X. Li, Q. Wang, Z. Zhu, T. Zhou, G. Wang, A. Xie, S. Luo, *Environ. Prog. Sustain.* **2022**, *42*, 13965.
[97] Y. Li, S. Liu, K. Yin, D. Jia, Y. Sun, X. Zhang, J. Yan, L. Yang, *J. Environ. Chem. Eng.* **2023**, *11*, 109050.
[98] B. Yuan, Y. Tao, S. Qi, A. Xie, S. Luo, *Environ. Sci. Pollut. Res. Int.* **2022**, *30*, 36993.
[99] S. Rousseau, S. Loridant, P. Delichere, A. Boreave, J. P. Deloume, P. Vernoux, *Appl. Catal., B* **2009**, *88*, 438.

[100] N. Parvizi, N. Rahemi, S. Allahyari, M. Tasbihi, E. Ghareshabani, *J. Taiwan Inst. Chem. Eng.* **2021**, *123*, 141.
[101] Y. Luo, K. Wang, Q. Chen, Y. Xu, H. Xue, Q. Qian, *J. Hazard. Mater.* **2015**, *296*, 17.
[102] X. Weng, W. L. Wang, Q. Meng, Z. Wu, *Catal. Sci. Technol.* **2018**, *8*, 4364.
[103] J. C. Tristao, J. D. Ardisson, W. A. A. Macedo, R. M. Lago, F. C. C. Moura, *J. Brazil Chem. Soc.* **2007**, *18*, 1524.
[104] A. Tarjomannejad, A. Farzi, A. Niaei, D. Salari, *Korean J. Chem. Eng.* **2016**, *33*, 2628.
[105] A. Rougier, S. Soiron, I. Haihl, L. Aymard, B. Taouk, J. M. Tarascon, *Powder Technol.* **2002**, *128*, 139.
[106] R. Pereñíguez, J. L. Hueso, J. P. Holgado, F. Gaillard, A. Caballero, *Catal. Lett.* **2009**, *131*, 164.
[107] C. Lv, J. Zhang, L. Yan, H. Chen, M. Hu, *J. Environ. Chem. Eng.* **2022**, *10*, 108372.
[108] M. Liu, X. Yang, Z. Tian, H. Wang, L. Yin, J. Chen, Q. Guan, H. Yang, Q. Zhang, *Phys. Chem. Chem. Phys.* **2022**, *24*, 3686.
[109] K. Ji, H. Dai, J. Deng, X. Li, Y. Wang, B. Gao, G. Bai, C. T. Au, *Appl. Catal., A* **2012**, *447–448*, 41.
[110] H. Huang, Z. Sun, H. Lu, L. Shen, Y. Chen, *React. Kinet., Mech. Catal.* **2010**, *101*, 417.
[111] H. Huang, Y. Liu, W. Tang, Y. Chen, *Catal. Commun.* **2008**, *9*, 55.
[112] S. A. Hosseini, D. Salari, A. Niaei, S. A. Oskoui, *J. Ind. Eng. Chem.* **2013**, *19*, 1903.
[113] M. Guo, K. Li, L. Liu, H. Zhang, X. Hu, X. Min, J. Jia, T. Sun, *J. Taiwan Inst. Chem. Eng.* **2019**, *102*, 268.
[114] J. G. Deng, L. Zhang, H. X. Dai, H. He, C. T. Au, *Ind. Eng. Chem. Res.* **2008**, *47*, 8175.
[115] J. Deng, L. Zhang, H. Dai, H. He, C. T. Au, *J. Mol. Catal. A: Chem.* **2009**, *299*, 60.
[116] X. Cui, H. Yang, J. Zhang, T. Wu, P. Zhao, Q. Guo, *Catal. Lett.* **2021**, *151*, 3323.
[117] H. Chen, G. Wei, X. Liang, P. Liu, Y. Xi, J. Zhu, *Catal. Sci. Technol.* **2020**, *10*, 5829.
[118] H. Chen, G. Wei, X. Liang, P. Liu, H. He, Y. Xi, J. Zhu, *Appl. Surf. Sci.* **2019**, *489*, 905.
[119] R. Pereñíguez, J. L. Hueso, F. Gaillard, J. P. Holgado, A. Caballero, *Catal. Lett.* **2012**, *142*, 408.
[120] J. A. Onrubia-Calvo, B. Pereda-Ayo, U. De-La-Torre, J. R. González-Velasco, *Appl. Catal., B* **2017**, *213*, 198.
[121] L. Guo, L. Bo, Y. Li, Z. Jiang, Y. Tian, X. Li, *Solid. State. Sci.* **2021**, *113*, 106519.
[122] M. Shetty, D. Zanchet, W. H. Green, Y. Roman-Leshkov, *ChemSusChem* **2019**, *12*, 2171.
[123] J. Li, J. Wang, H. Kuang, H. R. Zhang, Y. Y. Zhao, K. M. Qiao, F. Wang, W. Liu, W. Wang, L. C. Peng, Y. Zhang, R. C. Yu, F. X. Hu, J. R. Sun, B. G. Shen, *Nanoscale* **2017**, *9*, 13214.
[124] N. Parvizi, N. Rahemi, S. Allahyari, M. Tasbihi, *J. Ind. Eng. Chem.* **2020**, *84*, 167.
[125] K. Ji, H. Dai, J. Deng, H. Jiang, L. Zhang, H. Zhang, Y. Cao, *Chem. Eng. J.* **2013**, *214*, 262.
[126] L. Zhao, L. Jiang, Y. Huang, J. Zhang, J. Tang, C. Li, *Appl. Surf. Sci.* **2022**, *578*, 151977.
[127] Z. Zhao, H. Dai, J. Deng, Y. Du, Y. Liu, L. Zhang, *Microporous Mesoporous Mater.* **2012**, *163*, 131.
[128] J. Deng, Y. Zhang, H. Dai, L. Zhang, H. He, C. T. Au, *Catal. Today* **2008**, *139*, 82.
[129] J. Deng, L. Zhang, H. Dai, C. T. Au, *Catal. Lett.* **2009**, *130*, 622.
[130] Y. Zheng, K. Fu, Z. Yu, Y. Su, R. Han, Q. Liu, *J. Mater. Chem. A* **2022**, *10*, 14171.
[131] K. Kim, B. Koo, Y. Jo, S. Lee, J. Kim, B. Kim, W. Jung, J. Han, *Energy Environ. Sci.* **2020**, *13*, 3404.
[132] J. L. Hueso, J. P. Holgado, R. Pereñíguez, V. M. Gonzalez-DelaCruz, A. Caballero, *Mater. Chem. Phys.* **2015**, *151*, 29.
[133] A.-J. Ma, S.-Z. Wang, C. Liu, H. Xian, Q. Ding, L. Guo, M. Meng, Y.-S. Tan, N. Tsubaki, J. Zhang, L.-R. Zheng, X.-G. Li, *Appl. Catal., B* **2014**, *146*, 24.
[134] S. I. Suárez-Vázquez, S. Gil, J. M. García-Vargas, A. Cruz-López, A. Giroir-Fendler, *Appl. Catal., B* **2018**, *223*, 201.
[135] J.-M. Giraudon, A. Elhachimi, F. Wyrwalski, S. Siffert, A. Aboukaïs, J.-F. Lamonier, G. Leclercq, *Appl. Catal., B* **2007**, *75*, 157.
[136] F. Fang, P. Zhao, N. Feng, C. Chen, X. li, G. Liu, H. Wan, G. Guan, *Catal. Sci. Technol.* **2019**, *9*, 4938.
[137] R. M. Iqbal, S. D. Nurherdiana, M. S. Sahasrikirana, L. Harmelia, W. P. Utomo, E. P. Setyaningsih, H. Fansuri, *IOP Conf. Ser.: Mater. Sci. Eng.* **2018**, *367*, 012032.
[138] V. Dhongde, A. Singh, J. Kala, U. Anjum, M. A. Haider, S. Basu, *Mater. Rep.: Energy* **2022**, *2*, 100095.
[139] S. A. Oskoui, A. Niaei, H.-H. Tseng, D. Salari, B. Izadkhah, S. A. Hosseini, *ACS Comb. Sci.* **2013**, *15*, 609.
[140] G. Zhang, W. Dong, X. Huang, J. Zou, *Catal. Commun.* **2017**, *89*, 117.
[141] A. T. Kozakov, A. G. Kochur, V. G. Trotsenko, A. V. Nikolskii, M. El Marssi, B. P. Gorshunov, V. I. Torgashev, *J. Alloys Compd.* **2018**, *740*, 132.
[142] H. Vincent, M. Audier, S. Pignard, G. Dezanneau, J. P. Sénateur, *J. Solid State Chem.* **2002**, *164*, 177.
[143] Y. Xu, J. Dhainaut, J.-P. Dacquin, J.-F. Lamonier, H. Zhang, S. Royer, *Appl. Catal., B* **2024**, *342*, 123400.
[144] Y. Liu, W. Wang, X. Xu, J.-P. M. Veder, Z. Shao, *J. Mater. Chem. A* **2019**, *7*, 7280.
[145] J. Chen, X. Chen, N. Li, Y. Liang, C. Yu, L. Yao, Y. Lai, Y. Huang, H. Chen, Y. Chen, Z. Fan, *Ceram. Int.* **2021**, *47*, 19923.
[146] Y. Liu, H. Dai, J. Deng, L. Zhang, B. Gao, Y. Wang, X. Li, S. Xie, G. Guo, *Appl. Catal., B* **2013**, *140–141*, 317.
[147] Y. Liu, H. Dai, J. Deng, X. Li, Y. Wang, H. Arandiyan, S. Xie, H. Yang, G. Guo, *J. Catal.* **2013**, *305*, 146.
[148] X. Li, D. Chen, N. Li, Q. Xu, H. Li, J. He, J. Lu, *J. Alloys Compd.* **2021**, *871*, 159575.
[149] X. Li, H. Dai, J. Deng, Y. Liu, S. Xie, Z. Zhao, Y. Wang, G. Guo, H. Arandiyan, *Chem. Eng. J.* **2013**, *228*, 965.
[150] J. Zhang, L. Zhang, Y. Cheng, Y. Liu, *Fuel* **2023**, *332*, 126104.
[151] Z. Xie, J. Zhong, J. Tian, P. Liu, Q. Ren, L. Chen, M. Fu, D. Ye, *Appl. Catal., A* **2023**, *654*, 119069.
[152] X. Min, X. Wang, M. Guo, K. Li, J.-N. Gu, S. Hu, J. Jia, T. Sun, *Surf. Interfaces* **2023**, *38*, 102858.
[153] P. Wu, T. Chen, X. Jin, S. Zhao, Y. Chong, Y. Li, J. Lin, A. Li, Y. Zhao, Y. Qiu, D. Ye, *J. Hazard. Mater.* **2022**, *433*, 128765.
[154] X. Zhang, M. Zhao, Z. Song, H. Zhao, W. Liu, J. Zhao, Z.i' Ma, Y. Xing, *New J. Chem.* **2019**, *43*, 10868.
[155] Y. Liu, H. Dai, J. Deng, L. Zhang, Z. Zhao, X. Li, Y. Wang, S. Xie, H. Yang, G. Guo, *Inorg. Chem.* **2013**, *52*, 8665.
[156] S. Wang, Q. Liu, Z. Zhao, C. Fan, X. Chen, G. Xu, M. Wu, J. Chen, J. Li, *Ind. Eng. Chem. Res.* **2020**, *59*, 6556.
[157] L. Liu, J. Li, H. Zhang, L. Li, P. Zhou, X. Meng, M. Guo, J. Jia, T. Sun, *J. Hazard. Mater.* **2019**, *362*, 178.
[158] W. Si, Y. Wang, S. Zhao, F. Hu, J. Li, *Environ. Sci. Technol.* **2016**, *50*, 4572.
[159] X. Sun, D. Wu, *ChemistrySelect* **2019**, *4*, 5503.
[160] Y. Wang, Y. Xue, C. Zhao, D. Zhao, F. Liu, K. Wang, D. D. Dionysiou, *Chem. Eng. J.* **2016**, *300*, 300.
[161] M. Alifanti, M. Florea, V. I. Pârvulescu, *Appl. Catal., B* **2007**, *70*, 400.
[162] Y. Chen, K. Yao, X. Zhang, B. Shen, R. L. Smith, H. Guo, *J. Hazard. Mater.* **2022**, *436*, 129109.
[163] H. Yi, J. Xu, X. Tang, S. Zhao, Y. Zhang, Z. Yang, J. Wu, X. Meng, J. Meng, H. Yan, Q. Li, *Ultrason. Sonochem.* **2018**, *48*, 418.

[164] H. Yi, L. Miao, J. Xu, S. Zhao, X. Xie, C. Du, T. Tang, X. Tang, *Colloids Surf. A* **2021**, *623*, 126687.
[165] X. Wang, J. Zuo, Y. Luo, L. Jiang, *Appl. Surf. Sci.* **2017**, *396*, 95.
[166] R. Liu, B. Zhou, L. Liu, Y. Zhang, Y.u Chen, Q. Zhang, M. Yang, L. Hu, M. Wang, Y. Tang, *J. CColloid Interface Sci.* **2021**, *585*, 302.
[167] P. Kumar, A. Vijay Jagtap, S. Gupta, C. P. Vinod, *Chem. Asian J.* **2022**, *17*, 202200788.
[168] H. Hojo, Y. Inohara, R. Ichitsubo, H. Einaga, *Catal. Today* **2023**, *410*, 127.
[169] H. Einaga, N. Maeda, Y. Teraoka, *Appl. Catal., B* **2013**, *142–143*, 406.
[170] L. Deng, C. Huang, J. Kan, B. Li, Y. Chen, S. Zhu, S. Shen, *J. Rare Earths* **2018**, *36*, 265.
[171] L. Bao, D. Wu, *ChemistrySelect* **2021**, *6*, 7845.
[172] J. Yang, L. Li, X. Yang, S. Song, J. Li, F. Jing, W. Chu, *Catal. Today* **2019**, *327*, 19.
[173] Y. Wang, L. Xiao, C. Zhao, F. Liu, S. Li, *Environ. Prog. Sustainable Energy* **2018**, *37*, 215.
[174] Y. Tang, Y. Tao, T. Zhou, B. Yang, Q. Wang, Z. Zhu, A. Xie, S. Luo, C. Yao, X. Li, *Environ. Sci. Pollut. Res. Int.* **2019**, *26*, 36832.
[175] C. Lv, H. Chen, M. Hu, T. Ai, H. Fu, *Environ. Sci. Pollut. Res. Int.* **2021**, *28*, 37142.
[176] Y. Jiang, S. Xie, H. Yang, J. Deng, Y. Liu, H. Dai, *Catal. Today* **2017**, *281*, 437.
[177] Y. Jiang, J. Deng, S. Xie, H. Yang, H. Dai, *Environ. Sci. Pollut. Res. Int.* **2015**, *54*, 900.
[178] X.-H. Huang, X.-H. Shang, P.-J. Niu, *Acta Physico-Chimica Sinica* **2017**, *33*, 1462.
[179] J. Deng, L. Zhang, H. Dai, C.-T. I. Au, *Appl. Catal., A* **2009**, *352*, 43.
[180] M. Alifanti, M. Florea, G. Filotti, V. KUNCSER, V. Cortescorberan, V. Parvulescu, *Catal. Today* **2006**, *117*, 329.
[181] T. Shou, Y. Li, M. T. Bernards, C. Becco, G. Cao, Y. Shi, Y. He, *J. Hazard. Mater.* **2020**, *387*, 121750.
[182] L. Liu, B. Zhou, Y. Liu, J. Liu, L. Hu, Y. Tang, M. Wang, *J. Colloid. Interface. Sci.* **2022**, *606*, 1866.
[183] Z. Feng, Q. Ren, R. Peng, S. Mo, M. Zhang, M. Fu, L. Chen, D. Ye, *Catal. Today* **2019**, *332*, 177.
[184] X. Zhao, K. Sasaki, *Acc. Chem. Res.* **2022**, *55*, 1226.
[185] X. Li, Y. Wang, D. Chen, N. Li, Q. Xu, H. Li, J. He, J. Lu, *Green Energy Environ.* **2021**.
[186] L. Liu, H. Zhang, J. Jia, T. Sun, M. Sun, *Inorg. Chem.* **2018**, *57*, 8451.
[187] Y. Wang, S. Xie, J. Deng, S. Deng, H. Wang, H. Yan, H. Dai, *ACS Appl. Mater. Interfaces* **2014**, *6*, 17394.
[188] S. Chen, Y. Hao, R. Chen, Z. Su, T. Chen, *J. Alloys. Compd.* **2021**, *861*, 158584.
[189] M. Zang, C. Zhao, Y. Wang, X. Liu, Y. Cheng, S. Chen, *Appl. Surf. Sci.* **2019**, *483*, 355.
[190] K. Ji, H. Dai, J. Deng, L. Zhang, F. Wang, H. Jiang, C. T. Au, *Appl. Catal., A* **2012**, *425–426*, 153.
[191] J. Huang, K. Wang, X. Huang, J. Huang, *Mol. Catal.* **2020**, *493*, 111073.
[192] X. Liu, X. Lv, Y. Wang, C. Zhao, F. Liu, *J. Rare Earths* **2021**, *39*, 1073.
[193] B. Li, Y. Chen, L. Li, J. Kan, S. He, B. Yang, S. Shen, S. Zhu, *J. Mol. Catal. A: Chem.* **2016**, *415*, 160.
[194] N. Rezlescu, E. Rezlescu, P. D. Popa, C. Doroftei, M. Ignat, *J. Mater. Sci.* **2013**, *48*, 4297.
[195] X. Lv, T. Zhang, J. Cao, Y. Wang, F. Liu, L. Yin, *Environ. Sci. Pollut. Res. Int.* **2022**, *29*, 85202.
[196] Y. Liu, H. Dai, Y. Du, J. Deng, L. Zhang, Z. Zhao, C. T. Au, *J. Catal.* **2012**, *287*, 149.
[197] Y. Liu, H. Dai, Y. Du, J. Deng, L. Zhang, Z. Zhao, *Appl. Catal., B* **2012**, *119–120*, 20.
[198] K. Ji, H. Dai, J. Deng, H. Zhang, L. Zhang, H. Jiang, *Solid. State. Sci.* **2014**, *27*, 36.
[199] K. Ji, H. Dai, J. Deng, L. Song, B. Gao, Y. Wang, X. Li, *Appl. Catal., B* **2013**, *129*, 539.
[200] M. Alifanti, M. Florea, V. Cortes-Corberan, U. Endruschat, B. Delmon, V. I. Pârvulescu, *Catal. Today* **2006**, *112*, 169.
[201] H. Chen, W. Cui, D. Li, Q. Tian, J. He, Q. Liu, X. Chen, M. Cui, X. Qiao, Z. Zhang, J. Tang, Z. Fei, *Ind. Eng. Chem. Res.* **2020**, *59*, 10804.
[202] V. Blasin-Aubé, J. Belkouch, L. Monceaux, *Appl. Catal., B* **2003**, *43*, 175.
[203] J. Cao, X. Lv, Y. Huang, W. Jiang, Q. Kong, Y. Wang, *Colloids Surf. A* **2022**, *650*, 129509.
[204] K. Yu, T. Diao, J. Zhu, Z. Zhao, *Chem. Res. Chin. Univ.* **2018**, *34*, 119.
[205] Y. Wang, C. Wang, K. Zeng, S. Wang, H. Zhang, X. Li, Z. Wang, C. Zhang, *Appl. Surf. Sci.* **2022**, *576*, 151797.
[206] R. Wang, Y. Wang, M. Ren, G. Sun, D. Gao, Y. R. Chin Chong, X. Li, G. Chen, *Int. J. Hydrogen Energy* **2017**, *42*, 6757.
[207] P. Liu, Y. Liao, J. Li, L. Chen, M. Fu, P. Wu, R. Zhu, X. Liang, T. Wu, D. Ye, *J. Colloid Interface Sci.* **2021**, *594*, 713.
[208] C. Xu, S. Dong, T. Chen, H. Liu, X. Zou, M. Ji, Z. Han, D. Shu, C. Wang, D. Chen, *Fuel* **2023**, *347*, 128401.
[209] L.i Xiang, L. Zhang, J. Shao, F. Lin, Z. Wang, B. Yan, G. Chen, *J. Hazard. Mater.* **2023**, *441*, 129997.
[210] S. Wu, G. Wu, P. Wang, G. Guo, *Int. J. Hydrogen Energy* **2023**, *48*, 10288.
[211] S. V. Mazanov, Q. M. Phan, A. U. Aetov, Z. I. Zaripov, V. L. Starshinova, E. A. Karalin, R. A. Usmanov, F. M. Gumerov, I. M. Abdulagatov, *Symmetry* **2023**, *15*, 340.
[212] Y. J. Kim, D. Kim, Y. Kim, Y. Jeong, B. Jeong, J. Y. Park, *Int. J. Mol. Sci.* **2023**, *24*, 810.
[213] Z. Gu, H. Shen, L. Shang, X. Lv, L. Qian, G. Zheng, *Small Methods* **2018**, *2*, 1800121.
[214] J. Du, F. Li, L. Sun, *Chem. Soc. Rev.* **2021**, *50*, 2663.
[215] Y. Yu, M. Geng, D. Wei, C. He, *Acta Phys. Chim. Sin.* **2022**, *39*, 2206034.
[216] T. Yao, J. Long, Y. Duan, R. Gupta, Z. Xu, *J. Hazard. Mater.* **2023**, *450*, 131088.
[217] Y. Xuan, H. Gao, H. Tian, Z. Hu, J. Ma, Q. Yu, *Chem. Eng. J.* **2023**, *460*, 141592.
[218] S. Päivärinta-Antikainen, S. Ojala, S. Pitkäaho, L. Matějová, R. L. Keiski, *Resources* **2023**, *12*, 9.
[219] J. Huang, S. Wang, J. Gao, Y. Wang, C. Ma, G. Tian, H. Chen, *Environ. Pollut.* **2023**, *327*, 121540.
[220] W. Liang, G. Yin, X. Shi, J. Liu, F. Bin, *J. Environ. Eng.* **2023**, *149*, 04023009.
[221] H. Li, X. Peng, M. An, J. Zhang, Y. Cao, W. Liu, *Chem. Eng. J.* **2023**, *455*, 140751.
[222] R. Xie, L. Ma, Z. Li, Z. Qu, N. Yan, J. Li, *ACS Catal.* **2021**, *11*, 13119.
[223] J. Xia, Y.i Zhang, M. Cavazzini, S. Orlandi, B. Ding, H. Kanda, N. Klipfel, X.-X. Gao, Q. Ul Ain, V. Jankauskas, K. Rakstys, R. Hu, Z. Qiu, A. M. Asiri, H. Kim, P. J. Dyson, G. Pozzi, M. Khaja Nazeeruddin, *Angew. Chem., Int. Ed.* **2022**, *61*, 202212891.
[224] C. Liu, X. Sun, Y. Yang, Z. Shao, Y. Ding, Z. Fei, *Sci. Adv.* **2023**, 9.
[225] Y. Ding, B. Ding, H. Kanda, O. J. Usiobo, T. Gallet, Z. Yang, Y. Liu, H. Huang, J. Sheng, C. Liu, Y. Yang, V. I. E. Queloz, X. Zhang, J.-N. Audinot, A. Redinger, W. Dang, E. Mosconic, W. Luo, F. De Angelis, M. Wang, P. Dörflinger, M. Armer, V. Schmid, R. Wang, K. G. Brooks, J. Wu, V. Dyakonov, G. Yang, S. Dai, P. J. Dyson, et al., *Nat. Nanotechnol.* **2022**, *17*, 598.
[226] G. Li, Y. Hu, M. Li, Y. Tang, Z. Zhang, A. Musiienko, Q. Cao, F. Akhundova, J. Li, K. Prashanthan, F. Yang, P. Janasik, A. N. S. Appiah, S. Trofimov, N. Livakas, S. Zuo, L. Wu, L. Wang, Y. Yang, B. Agyei-Tuffour, R. W. MacQueen, B. Naydenov, T. Unold, E. Unger, E. Aktas, S. Eigler, A. Abate, *Angew. Chem., Int. Ed.* **2023**, *62*, 202307395.

[227] P. Tyagi, D. Singh, N. Malik, S. Kumar, R. Singh Malik, *Mater. Today* **2023**, *65*, 133.
[228] M. Tawalbeh, R. Muhammad Nauman Javed, A. Al-Othman, F. Almomani, *Energy Convers. Manage.* **2023**, *279*, 116755.
[229] C. H. Bartholomew, *Appl. Catal., A* **2001**, *212*, 17.
[230] H. Wang, P. Tian, Z. Chen, S. Wu, W. Yang, Q. Yu, J. Zhou, *Chem. Eng. Commun.* **2018**, *206*, 22.
[231] M. Ghafari, J. D. Atkinson, *Polymer* **2017**, *116*, 278.
[232] J. Pu, H. Wang, M. Suzuki, E. W. Qian, *RSC Adv.* **2021**, *11*, 20570.

**Jianhua Yuan** is currently pursuing his Ph.D. degree in College of Environmental Science and Engineering at Tongji University under the guidance of Prof. Jie Ma. He received his B.E. (2017) in biological engineering at Chongqing University of Technology, and M.S. (2019) in environmental science and engineering at the University of Chongqing. His research interests mainly focus on microbial synthesis of nanomaterials, catalytic oxidation and water environmental pollution control.

**Guixiang Li** is a postdoctoral researcher in the Institute of Chemical Sciences and Engineering at the Ecole Polytechnique Fédérale de Lausanne (EPFL). He completed his Ph.D. from Helmholtz-Zentrum Berlin für Materialien und Energie (HZB) in 2023. His current research interests are focused on the stabilization mechanism of perovskite materials and solar cells and processing high-quality tin-containing perovskites for optoelectronic devices.

**Zhaofu Fei** is a senior research scientist in the Institute of Chemical Sciences and Engineering at the EPFL. He received his Ph.D. degree from the Technical University of Braunschweig, Germany in 1999. After postdocs in the UK and Germany he joined EPFL in 2002. His research interests are focused on design and synthesis of ionic liquids and related nanomaterials.

**Jie Ma** is a professor in College of Environmental Science and Engineering at Tongji University. He received an M.S. degree from Hefei University of Technology in 2005, a Ph.D. degree from Shanghai Jiaotong University in 2009, and as a visiting scholar in Department of Chemical & Biomolecular Engineering at the University of Akron in 2015-2016. His current research focuses on nanomaterial innovations and electrochemical technology for sustainable environment.

**Mohammad K. Nazeeruddin** is a professor of chemistry at the EPFL, and his research focuses on perovskite and dye-sensitized solar cells and light-emitting diodes. His group is involved in developing stable perovskite solar cells by compositional and interface engineering and developing novel hole-transporting materials. He received his Ph.D. degree in inorganic chemistry from Osmania University Hyderabad, India. He was appointed as World Class University (WCU) professor at Korea University, and Adjunct Professor at King Abdulaziz University, Jeddah.

**Paul J. Dyson** is a professor in the Institute of Chemical Sciences and Engineering at the EPFL. He received his Ph.D. degree from the University of Edinburgh in 1993 and subsequently held positions at Imperial College of Science, Technology and Medicine and the University of York. His research interests are focused on synthesis and properties of compounds and materials with applications in catalysis and medicine.